Energy & Environmental Science

# Two-dimensional non-layered materials for electrocatalysis



| | |
|---|---|
| Journal: | *Energy & Environmental Science* |
| Manuscript ID | EE-REV-05-2020-001714.R2 |
| Article Type: | Review Article |
| Date Submitted by the Author: | 22-Sep-2020 |
| Complete List of Authors: | Wang, Yizhan; University of Wisconsin Madison,<br>Zhang, Ziyi; University of Wisconsin Madison<br>Mao, Yanchao; Zhengzhou University,<br>Wang, Xudong; University of Wisconsin, 213 Materials Science and Engineering |
| | |

REVIEW

# Two-dimensional non-layered materials for electrocatalysis

Yizhan Wang,[a] Ziyi Zhang,[a] Yanchao Mao*[b] and Xudong Wang*[a]

Received 00th January 20xx,
Accepted 00th January 20xx

DOI: 10.1039/x0xx00000x

Abstract: Creating two dimensional (2D) geometry from non-layered catalytic materials may significantly advance electrocatalysts design. 2D morpohology of three dimensional lattices (2D non-layered materials) offer large structure distortions, massive surface dangling bonds, and coordinated-unsaturated surface atoms, which can induce high surface chemical activity, promote chemisorption of reactants and fast interfacial charge transfer, and thus enhance electrocatalytic performance. In this article, we review typical strategies for structure engineering and electronic states manipulation to enable the unique electrocatalytic advantages of 2D non-layered materials. An overview is presented on recent research advances in the development of 2D non-layered materials for catalyzing representative electrochemical reactions that are essential to energy and sustainability, including hydrogen evolution, oxygen evolution, oxygen reduction, and $CO_2$ reduction. For each type of redox reactions, their unique catalytic performance and underlying mechanism are discussed. Important achievements and key challenges are also pointed out.

## 1. Introduction

Two-dimensional (2D) nanomaterials have attracted extensive research interests in recent years and are now playing a key role in materials innovation and property advancement.[1-4] The family of 2D nanomaterials have rapidly expanded from graphene to carbon nitrides,[5-14] transition-metal dichalcogenides (TMDs),[15] Xenes,[16] black phosphorus,[17] hexagonal boron nitride,[18] metal–organic frameworks[19] and their heterostructures.[20, 21] In contrast to their bulk counterparts and other forms of nanostructures, 2D nanomaterials with a thickness of just one or a few atomic layers, could show unique optical, electrical, chemical and mechanical properties, leading to broad application potentials in photovoltaics, catalysts, sensors, and thermoelectrics.[4, 22-24] Thus far, study of 2D nanostructures are largely limited to naturally layered materials, *i.e.* the van der Waals (vdW) solids. These solids have strong in-plane chemical bonds but weak out-of-plane vdW bonds, and thus can be readily produced either from top-down methods, like exfoliation by micromechanical cleavage[25], ionic intercalation in solution[26] and ultrasonication,[27] or from bottom-up methods, such as chemical vapor deposition.[3, 28, 29] Their 2D atomic lattices give rise to ultrahigh specific surface area, enhanced electronic conductivity, and short electron/carrier transfer distance. These intriguing structural and electronic properties of 2D nanomaterials bring in numerous potentials for electrocatalysis applications. Currently, a broad range of 2D nanomaterials as advanced electrocatalyst have been comprehensively discussed in a number of review articles.[30-34]

Nevertheless, many traditional high-performance electrocatalysts, such as precious metal (e.g. Pt, Pb) and metal oxides (e.g., $RuO_2$, $IrO_2$), all have a non-layered crystal structure with intrinsic isotropic chemical bonds in three dimensions. Compared to vdW solids, creating 2D geometry from these non-layered catalytic materials may offer greater impacts for catalysts design (**Figure 1**). First, 2D non-layered materials may subject to large structure distortion with massive surface dangling bonds, which is not common in layered materials, enabling highly chemically active surfaces and enhanced catalytic performance. Second, the exposed surface atoms with low coordination numbers can promote chemisorption of reactants and induce fast interfacial charge transfer. Third, the structural and electronic properties of 2D non-layered materials can be tuned by structure and surface engineering, which can further tailor the catalytic performance. Moreover, defects (e.g. vacancies) are always associated with the 2D lattices, which offer additional influences to the surface electronic structure and charge transport properties. Fundamentally, the ultrathin 2D geometry provides an ideal and relatively simple platform to study the catalytic mechanisms at the atomic level, as well as to model the electronic-state modulation for establishing reliable structure–property relationships.

Different from 2D vdW solids, creating 2D morphology from non-layered materials typically requires stabilization of crystal phases or structures far away from thermodynamic equilibrium. Control of kinetics must be introduced to break the crystal symmetry and foster 2D anisotropy in crystal growth. To realize the anisotropic growth of non-layered materials, a number of synthesis strategies for synthesizing 2D morphology from a broad range of materials – beyond those bonded by vdW interactions – have been developed, including ionic layer

[a] Department of Materials Science and Engineering, University of Wisconsin-Madison, Madison, WI 53706, USA. Email: xudong.wang@wisc.edu
[b] Key Laboratory of Materials Physics, Ministry of Education, School of Physics and Microelectronics, Zhengzhou University, Zhengzhou 450001, China. Email: ymao@zzu.edu.cn

Electronic Supplementary Information (ESI) available: [details of any supplementary information available should be included here]. See DOI: 10.1039/x0xx00000x

epitaxy,[35] oriented attachment,[36] lamellar intermediate-assisted exfoliation,[37, 38] 2D template synthesis,[39] and topochemical transformation.[40] Enabled by these novel synthesis strategies, a broad range of 2D non-layered materials have been successfully developed including metals, metal oxides, metal chalcogenides, transition metal dichalcogenides, metal nitrides, metal phosphides and many others.[41] Due to their lacking of intrinsic layered configuration, these materials usually exhibited a thickness of at least a few layers of unit cells (*i.e.* in the range of 0.5 nm to >10 nm). Therefore, they should be more accurately termed as quasi-2D nanomaterials. To make it simple, in this article, they are all termed as 2D non-layered materials or followed by specific material names. Representative synthesis strategies for 2D non-layered materials have been well documented in a few recent reviews.[1, 41, 42] Leading by the blooming of various 2D non-layered materials, promising results have also been demonstrated in advancing the electrocatalysis applications by this new family of 2D nanomaterials. Nevertheless, despite the remarkable initial successes in 2D non-layered materials for electrocatalysis, there lacks comprehensive reviews focusing on the promising catalytic behavior related to the 2D lattices of non-layered materials. In this article, we will provide a systematic overview of recent research advances in the development of 2D non-layered materials for electrocatalysis applications. First, we will introduce strategies for structure engineering and electronic states manipulation of 2D non-layered materials enabling their unique advantages as electrocatalysts. Afterwards, we will discuss the applications of 2D non-layered materials for catalyzing four representative categories of electrochemical reactions that are essential to energy and sustainability, including hydrogen evolution reaction (HER), oxygen evolution reaction (OER), oxygen reduction reaction (ORR), and $CO_2$ reduction reaction. For each reaction, their unique catalytic performance and underlying mechanism will be described. At last, we will conclude with a summary of important achievements and an outlook on the key challenges in this field.

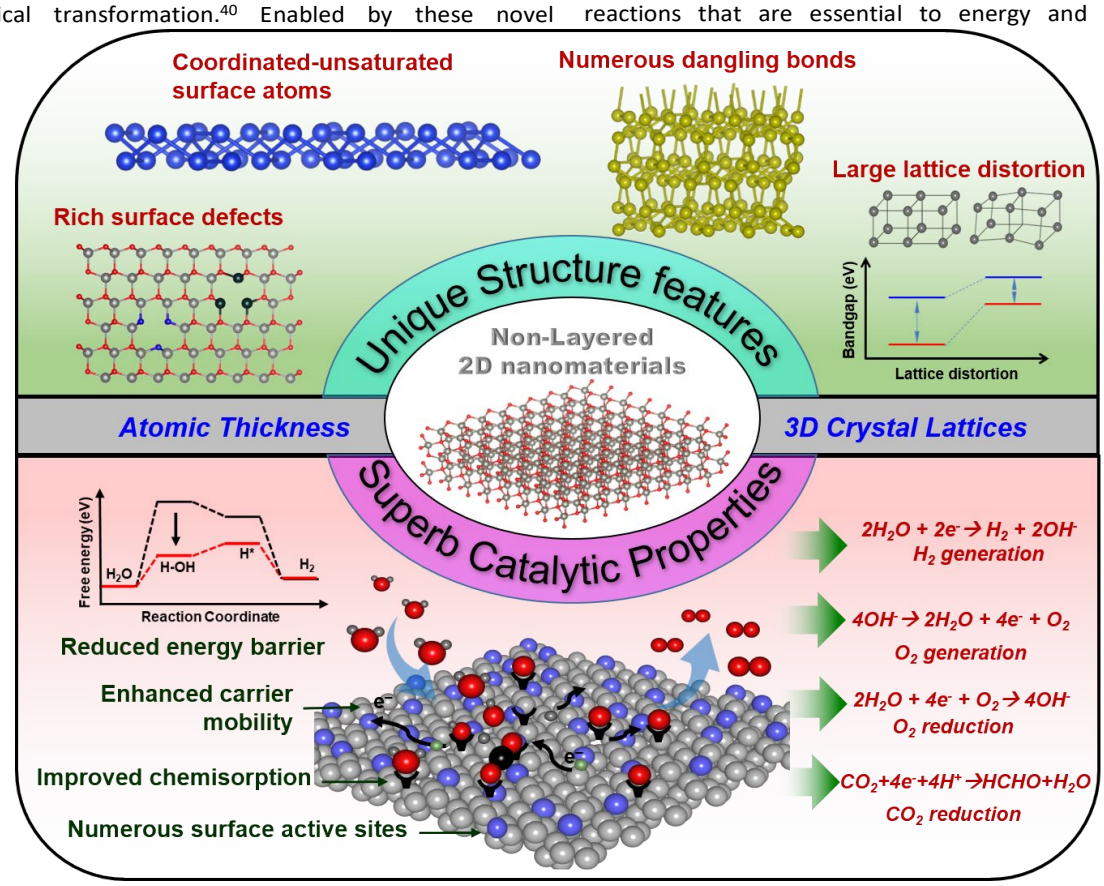


**Figure 1.** Unique structure features and associated superb catalytic properties of 2D non-layered materials for their applications towards HER, OER, ORR and $CO_2$ reduction.

## 2. Structure engineering of 2D non-layered electrocatalysts

The intriguing advantages of 2D nanomaterials for electrocatalysis are primarily related to their unique morphology and atomic structures. In this section, we will discuss how to control a few key parameters of 2D non-layered materials, including thickness, point defects (vacancies and doping) and heterogeneity, and their influences to electrocatalysis applications.

### 2.1 Thickness control

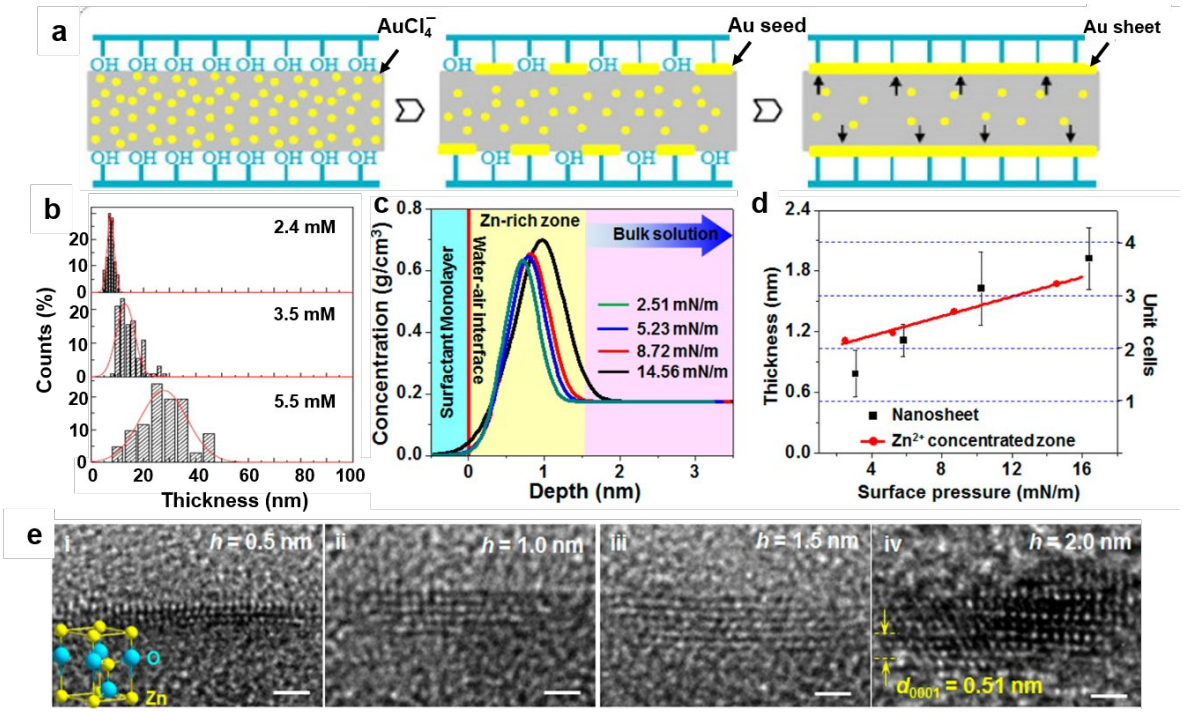


**Figure 2.** Thickness control of 2D non-layered materials. (**a**) Schematic illustration of the synthesis procedure of 2D Au. (**b**) Thickness distribution histograms corresponding to different $HAuCl_4$ concentrations. [47]Reproduced with permission from © 2013 American Chemical Society. (**c**) $Zn^{2+}$ ion concentration profiles underneath the surfactant monolayer with four different surface pressures. Sky blue represents the surfactant monolayer. Light yellow represents the Zn-concentrated zone (the Stern layer). Lavender represents the bulk solution. (**d**) Plots of the thickness (black squares) and the width of Zn-concentrated zone (red dots) as functions of the surface pressure. The numbers of ZnO unit cell are highlighted by dashed blue lines. (**e**) Cross-sectional HRTEM images of 2D ZnO with a thickness from one to four unit cells. Inset shows one unit cell of wurtzite ZnO. [44]Reproduced with permission from © 2017 American Chemical Society.

Controlling the materials thickness down to the nanometer scale is one of the most effective ways to modulate the electronic structure and chemical activities. When the thickness of a semiconductor material reduced to a few or a single atomic layer, the bandgap would be broadened due to the quantum confinement effect. The electronic density of state (DOS) can also largely increase at the surface of a 2D material compared to those in the interior of a bulk structure. In addition, the reduced thickness could induce surface lattice distortion[43] and electronic structure changes such as lowering the work function, indicating a potential to achieve tunable band alignment in electrocatalysis design.[44] Furthermore, the ratio of exposed surface atoms sharply increases as the thickness reduces to the nanometer scale, leading to enhanced surface effect. Due to the lack of neighboring atoms, abundant low coordination surface atoms with dangling bonds will form. To maintain the structural stability, these surface atoms are prone to bond with other atoms or molecules, and thus display much improved chemical activity.[32] In a representative example, the catalytic performance of 2D $SnO_2$ with different thicknesses was compared for carbon monoxide oxidation.[45] Because the sub-nanometer-thick 2D $SnO_2$ had a larger fraction of low coordinated surface atoms and a higher DOS compared to thicker $SnO_2$ nanosheets and bulk $SnO_2$, it exhibited remarkably improved CO catalytic performances, with the activation energy lowered to 59.2 $kJmol^{-1}$ from 121.1 $kJmol^{-1}$ and the CO full-conversion temperature reduced by over 200 °C.

Nevertheless, different from layered crystal structures, where the thickness can be relatively easily controlled by the number of atomic layers, controlling the thickness of 2D non-layered materials is rather challenging due to the lack of a significant driving force for 2D anisotropic growth. In the 2D $SnO_2$ catalysts mentioned above, the thickness was controlled by the growth temperature. 2D $SnO_2$ with an average thickness of 0.66 nm were synthesized at 180 °C for 48 h in a solvothermal reaction between $SnCl_2 \bullet 2H_2O$ and ethylenediamine. A higher temperature of 220 °C yielded a larger average thickness of ~1.9 nm.[45] This is a relatively common growth phenomenon that a higher temperature would lead to faster growth rate, and thus weaken the anisotropy in 2D morphology.[46] In wet-chemistry systems, the concentration of precursors was also found able to control the thickness. Typically, higher precursor concentration would promote a more isotropic growth of 2D materials leading to larger thickness after the possible Ostwald ripening process (**Figure 2a-b**).[47-49,] As exampled by a graphene oxide-templated synthesis strategy, a range of binary oxides (including MgO, $ZrO_2$, $Al_2O_3$, $TiO_2$, $SnO_2$, and $Sb_2O_5$) were grown into 2D morphology with a thickness of several nanometers. The thickness of these 2D layered materials were tuned by the concentration of metal precursors.[50]

Despite a wide range of thickness control strategies by varying the reaction conditions, it was rarely reported that the thickness of 2D non-layered materials could be tuned down to

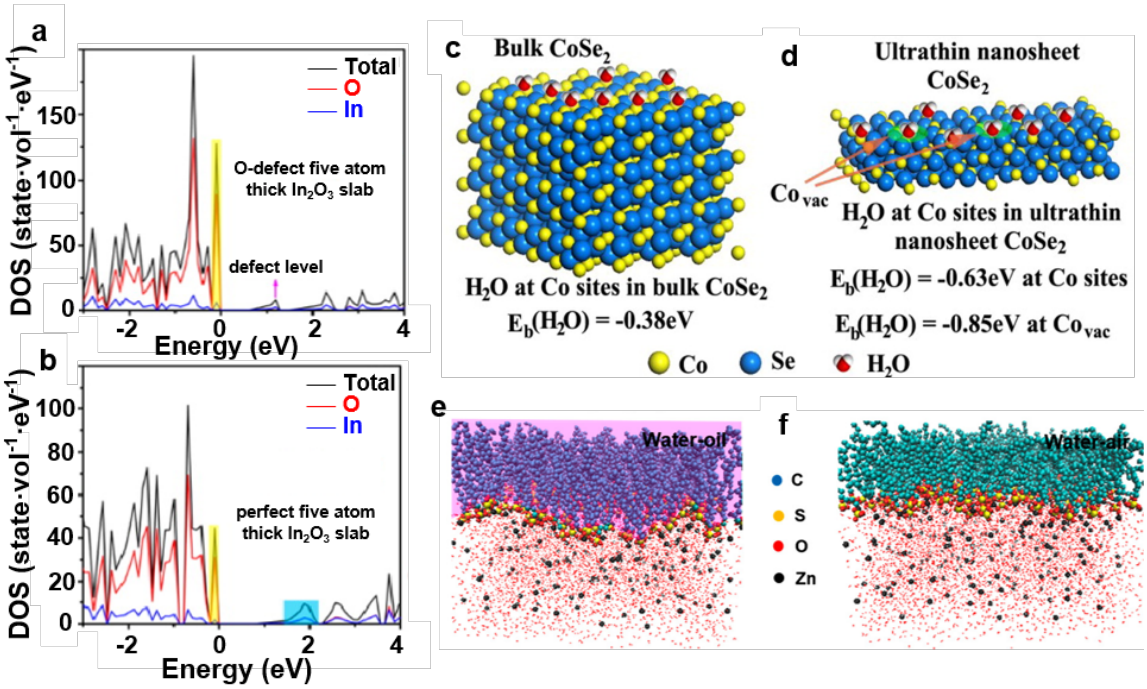


**Figure 3.** Vacancy manipulation of 2D non-layered materials. (**a**) Calculated DOS of oxygen-defect 5-atom-thick $In_2O_3$ slab. (**b**) Calculated DOS of perfect 5-atom-thick 2D $In_2O_3$. [57]Reproduced with permission from © 2014 American Chemical Society. First-principles study of surface $H_2O$ adsorption on different sites and performance of various materials: (**c**, **d**) Geometries and binding energies of $H_2O$ molecules on cobalt sites and vacancies. [58]Reproduced with permission from © 2014 American Chemical Society. MD simulation generated $Zn^{2+}$ ion distribution at (**e**) water–air and (**f**) water–oil interfaces. [62]Reproduced with permission from © 2019 American Chemical Society.

a single atomic layer. One technology that distinguishes from the others with the capability of unit-cell level thickness control is ionic layer epitaxy (ILE). It was recently developed as an effective strategy to synthesizing 2D non-layered materials, such as ZnO[35, 51], Pd[52], and CoO[53, 54] that are promising electrocatalysts. This technology used surfactant monolayers at water/air interface as a soft template to guide the growth of 2D materials, where the packing density of the surfactant was discovered as the key parameter for thickness control. Based on the example 2D ZnO growth system, molecular dynamics (MD) simulations revealed that both the $Zn^{2+}$ concentration and the width of the $Zn^{2+}$ concentrated zone (the Stern layer) underneath the surfactant monolayer increased monotonically with increasing surfactant packing density (**Figure 2c**). Comparing experimental measurements with the simulation results revealed an excellent match between the thickness and the Stern layer width, confirming the direct relationship between the thickness of the Stern layer and the thickness of the 2D materials (**Figure 2d**). As the surface pressure was adjusted from 3.09 to 16.40 mN/m, 2D ZnO with one to four unit cell thickness were achieved (**Figure 2e**). This self-limited thickness control in ILE brings up a new capability for precision thickness control of 2D non-layered material synthesis, which may enable more quantitative study on 2D electrocatalysis.

### 2.2 Vacancy manipulation

Cation and anion vacancies are a well-known factor that controls the materials physical and catalytic properties, such as electronic structure, carrier concentration, electrical conductivity and atom coordination. As a result of the intrinsic 3D crystal lattices, vacancies are commonly presented in 2D non-layered materials, and might bring significant impacts to the catalysis performance. For example, the Sn/O dual vacancies in 2D $SnO_2$ could evolve into isolated Sn vacancy under a relatively small electric field, which would induce reversible transition between semiconductor and half-metal accompanied by an abrupt conductivity change up to $10^3$ times. DFT calculations further revealed that 2D $SnO_2$ with Sn/O dual vacancies would show semiconductive behavior; while isolated Sn vacancy would induce a half-metallic characteristic, mostly originating from the O 2p state.[55, 56] DFT calculation also revealed that presence of O-vacancies in 2D $In_2O_3$ could increase DOS at the valence band edge and lead to a new defect level in the forbidden band (**Figure 3a, b**).[57] The change of electronic structure suggested that electrons can be more easily excited into the conduction band, and thus the O-vacancy-rich 2D $In_2O_3$ would possess a higher carrier concentration than that of a perfect lattice. In addition, the physicochemical properties can also be tailored by vacancies. It was reported that Co vacancies in 2D $CoSe_2$ could serve as active sites to catalyze OER (**Figure 3c, d**).[58] DFT calculations showed that Co vacancies in 2D $CoSe_2$ would exhibit a water molecule adsorption energy of 0.85 eV, larger than that of cobalt sites in bulk $CoSe_2$ (0.38 eV), indicating that Co vacancies in an ultrathin structure could be more favorable for adsorbing $H_2O$ and catalyzing OER.

Commonly, vacancies could be created and tuned in multiple ways in bulk crystals, where most of them could be readily adapted to 2D non-layered materials. Fast heating phase transformation is a powerful approach to engineering surface defects.[57, 59-61] As a typical example, starting with ultrathin

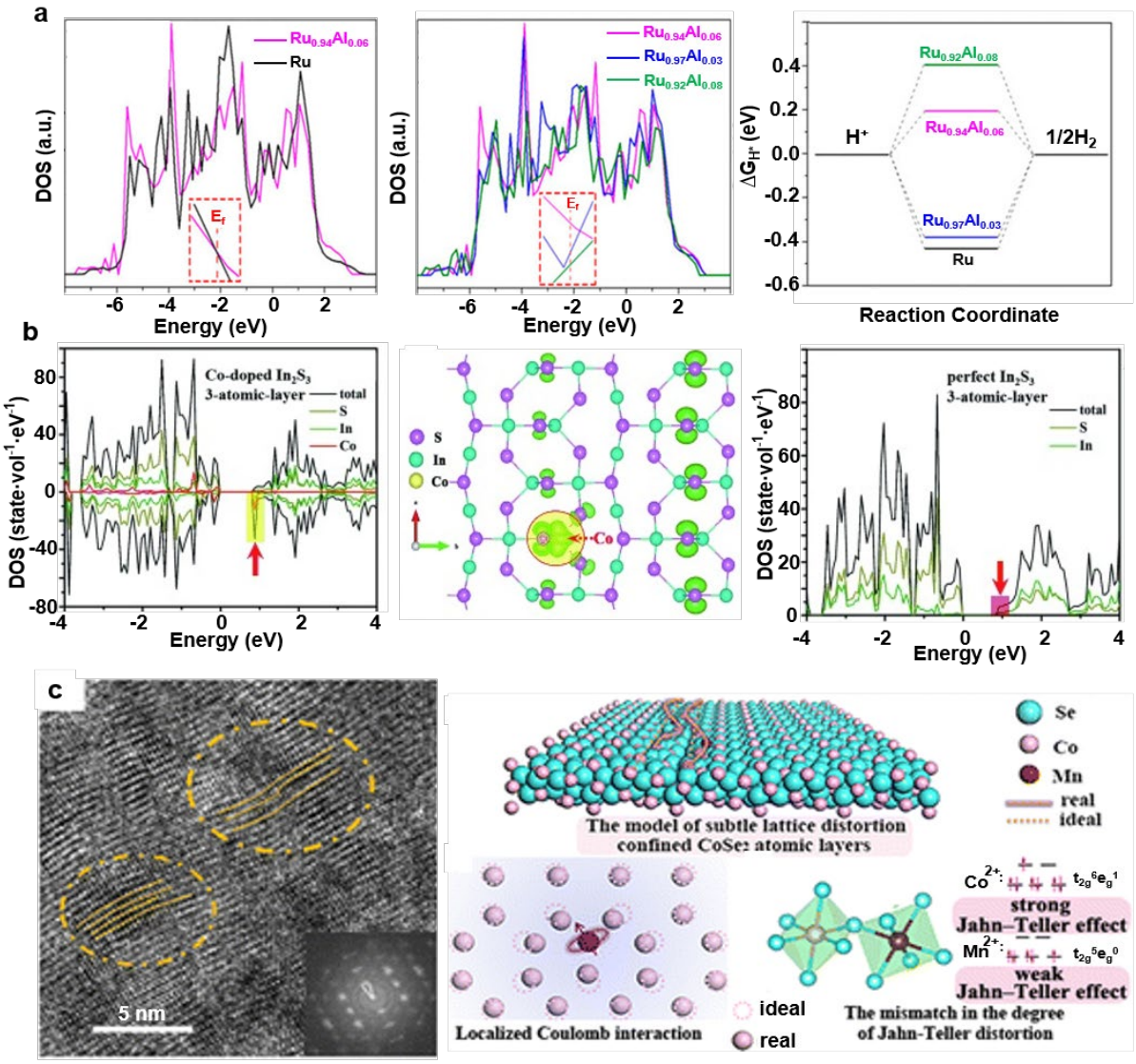


**Figure 4.** Elemental doping of 2D non-layered materials. (**a**) DFT calculated DOSs and HER free-energy diagrams of pristine and Al-doped 2D Ru. [64]Reproduced with permission from © Copyright 2019 American Chemical Society. (**b**) DFT calculated DOSs and charge-density distribution of the conduction band edge of Co-doped and pristine 2D $In_2S_3$ with 3-atomic-layer thickness. [65]Reproduced with permission from © 2015 Wiley-VCH Verlag GmbH & Co. KGaA, Weinheim. (**c**) HRTEM images and corresponding FFT patterns (insets) for Mn doped 2D $CoSe_2$ with schematic representations of the formation mechanism for the subtle distortion of atomic arrangement through the incorporated heterogeneous spin states. [66]Reproduced with permission from © Copyright 2016 American Chemical Society.

$In(OH)_3$, fast heating at 400 °C for 3 min yielded 2D $In_2O_3$, where the concentration of O-vacancies was controlled by the oxygen partial pressure of the calcination atmosphere.[57] As a kinetically controlled synthesis approach, the ILE technique is also versatile in controlling the evolution of defects within a quasi 2D crystal lattice. By introducing a water-oil interface, polycrystalline 2D ZnO with an unprecedented Zn vacancy concentration of up to ~33% were synthesized (**Figure 3e, f**). Stabilizing such a high Zn vacancy concentration was attributed to local charge balancing in the ultrathin geometry from the surfactants and the fast growth kinetics.[62] In addition, plasma treatment has been demonstrated as an efficient strategy to introduce surface vacancies. For example, Ar plasma on 2D $Co_3O_4$ could partial reduce $Co^{3+}$ to $Co^{2+}$, producing oxygen vacancies. The synergistic effect of the surface oxygen vacancies and high surface area of 2D $Co_3O_4$ could largely enhance the electrocatalytic activity.[63]

### 2.3 Elemental Doping

Extrinsic point defects, represented by elemental dopants, could induce many intriguing physical and chemical alterations, such as distortion in atomic arrangement, redistribution of electron density, increasing of delocalized electrons, and exposure of more active sites, providing opportunities to manipulate 2D materials for enhanced catalytic applications. For instance, Zhang *et al*. effectively regulated the electronic structure of 2D Ru and enhanced the HER activity by Al doping.[64] DFT calculation depicted that the basal plane of Al-doped 2D Ru exhibited more delocalized electron distribution than pristine 2D Ru, raising the number of active sites on 2D Ru for HER (**Figure 4a**). Besides, more states at the valence band edges could accelerate electron transfer from the catalyst surface to the

adsorbed $H^+$ facilitating the reduction. Al doping also reduced the Gibbs free energy for hydrogen adsorption improving the catalytic performance.

Confined doping in atomic layers was recently reported as an effective approach in moderating the catalytic properties of 2D non-layered materials. It confined doping elements in the basal planes of the material, while maintaining the 2D atomic arrangement and electron conjugated system. This strategy could yield an excess of catalytic active sites, providing an opportunity to regulate the electronic structure to optimize the electrocatalytic dynamics. Confined Co doping in three atomic layers of $In_2S_3$ brought several new energy levels due to the splitting of Co 3d states, hence achieved significant improvement in photocatalytic activity.[65] DFT calculations showed that vast majority of charge density was originated from the Co and S atoms (**Figure 4b**), suggesting that most of the confined Co dopants could directly involve in the photocatalytic reaction facilitating easier electron excitation by the d-d internal transitions of Co ions under light. The presence of Co dopant also endowed 2D $In_2S_3$ with obviously increased DOS at the conduction band minimum, which allowed for higher carrier density and efficient carrier transport along the 2D conducting channels. Through a similar approach, Mn was doped into the primitive lattice of 2D $CoSe_2$, introducing subtle atomic distortion and heterogeneous spin states in the atomically thin lattices (**Figure 4c**).[66] The variation of the electronic structure could lower the kinetic energy barrier by promoting H−H bond formation on two adjacently adsorbed H atoms, and thus enhanced the HER performance.

In general, this section summarizes three important and unique structural factors, *e.g.* thickness, intrinsic defects (vacancies) and extrinsic defects (dopants) in 2D non-layered materials, and discusses how they were controlled and fundamentally correlated to catalytic performance. In the following sections, we will discuss specific examples of non-layered 2D materials revealing how their ultrathin geometry is correlated to four representative catalytic processes, i.e. HER, OER, ORR and $CO_2$ reduction.

## 3. Hydrogen Evolution Reaction

Hydrogen fuel cell is a critical technology in clean and renewable energy application. The main source of high purity hydrogen is from electrocatalytic water splitting, where HER is the cathodic reaction in water electrolysis producing $H_2$. The thermodynamic potential needed to drive water electrolysis is 1.23 V (versus Reversible Hydrogen Electrode, RHE), while the practical voltage applied to drive water electrolysis is usually larger than this value due to the Ohmic drop and the overpotential associated with reactions on the anode and cathode. HER is a two-electron transfer reaction with multiple steps including adsorption, reduction, and desorption. The adsorption of hydrogen (H*) on the catalyst surface typically occur through the Volmer process, which is then reduced forming molecular hydrogen *via* either a Heyrovsky or Tafel step.[30] During a HER, the hydrogen adsorption energy typically plays the most significant role in determining the rate of the overall reaction, and is the key to consider in catalyst development.[56] HER catalysis is one of the most promising applications for 2D non-layered materials, which have showed comparable catalytic activities to Pt-based catalysts. They share many common advantages as a high-performance catalytic material, including very large surface area, numerous low-coordinated atoms for hydrogen adsorption, and improved electrical conductivity and carrier mobility. These advanced features could be further tuned to enhance the electrocatalytic performances *via* material structure engineering. So far, a variety of 2D non-layered materials has been studied for HER electrocatalysis including metals, transition metal chalcogenide, metal phosphides and metal nitrides. In contrast, 2D layered materials, such as Graphene and TMDs, intrinsically show relative low activity towards the HER electrocatalysis due to their mostly coordinated surface. The basal plane of pure graphene is inert for the HER with a relatively large (positive) $\Delta G_H$* (1.85 eV). To improves its HER performance, elements with different electronegativity, such as N, P, S, have to be doped into the carbon matrix of graphene to induce the redistribution of charge/spin to graphene layer. For layered TMDs, the HER performance is largely limited by the density of active sites, which are concentrated at the layer edges. Accordingly, significant research efforts have been directed towards synthesis strategies that can expose additional active edge sites to enhance overall performance. Strategies like heteroatom doping, defect engineering, interaction engineering, etc. have been used to tune its $\Delta G_H$* and band structure for enhanced activity. A chronological summary of different 2D non-layered catalysts and their characteristic parameters reported for HER is shown in **Table 1**. Here, we will discuss the advanced HER performance of 2D non-layered materials in these material groups together with representative strategies to improve their performance.

### 3.1. Metals

A number of noble metals are well-known excellent catalytic materials for HER. However, their strong preference for close-packed crystalline structures and rich dangling bonds would make 2D metal materials extremely active and unstable.[67] Thus, it remained a big challenge to synthesis 2D metals, although the 2D morphology are expected to exhibit extraordinary catalytic property.[68, 69] Kong *et al.* used a solvothermal method to synthesize free-standing 2D Ru with a thickness of 1.0-1.2 nm *via* oriented attachment. In this approach, isopropanol was used as the solvent to guide the anisotropic Ru growth. Meanwhile, urea was introduced as the selective capping reagent to prevent colloidal aggregation and direct the attachment into a large 2D geometry (**Figure 5a**).[70] The 2D structure exhibited enhanced HER activities compared to Ru powder counterparts (**Figure 5b)** with an onset potential comparable to the value for commercial Pt/C. The overpotential was reduced to 20 mV at a current density of 10 mA $mg^{-1}$ and a Tafel slope of 46 mV $dec^{-1}$. DFT calculation indicated that the enhanced HER activity from 2D Ru could be attributed to the smaller free energy change $|\Delta G_H|$ for hydrogen adsorption at the hollow sites on Ru (001) (**Figure 5c**). Nevertheless, surface capping ligands were always undesirable as they block the sites or routes for hydrogen adsorption. To realize non-ligand-caped 2D metal materials, Kuang *et al.* reported an *in situ* topotactic reduction method to synthesize 2.2-nm 2D nickel arrays from $Ni(OH)_2$. The partial oxidization of 2D Ni resulted impressive HER activities with a Tafel slope of 114 mV $dec^{-1}$, smaller than that of the Ni/NiO nanoparticles counterpart (135 mV $dec^{-1}$).[71]

REVIEW

**Table 1.** Summary of 2D non-layered materials reported for HER electrocatalysts.

| Catalyst | Electrolyte | Synthetic method (precursor) | Thickness | Overpotential (mV) (10 mA $cm^{-2}$) | Tafel slope (mV $dec^{-1}$) | Refs., year |
|---|---|---|---|---|---|---|
| Ru | 0.5 M $H_2SO_4$ | Solvothermal method with $Ru(acac)_3$ and Urea | 1.0–1.2 nm | 20 | 46 | [70], 2016 |
| Ni | 0.1 M KOH | Topotactic reduction of $Ni(OH)_2$ | 2.2 nm | Onset potential of 34 mV | 114 | [71], 2016 |
| Pt/Cu | 0.05 M $H_2SO_4$ | CO-assisted method with $Pt(acac)_2$, $Cu(acac)_2$ and PVP | 1.6 nm | 55 (100 mA $cm^{-2}$) | 23 | [72], 2016 |
| Ni–Mo alloy | 1.0 M KOH | Topotactic reduction of $NiMoO_4$ | 2 nm | 35 | 45 | [73], 2017 |
| PtAgCo | 0.5 M $H_2SO_4$ | Oxidative etching strategy with $Co(acac)_2$ $Pt(acac)_2$, and $AgNO_3$ | - | 705 mA $cm^{-2}$ at −400 mV | 27 | [74], 2017 |
| PdCu alloy | 1.0 M KOH | CO-assisted method with $Na_2PdCl_4$ and $CuCl_2$ | 1.8 nm | 106 | 124 | [75], 2017 |
| $NiSe_2$ | 0.5 M $H_2SO_4$ | Topotactic conversion with β-2D $Ni(OH)_2$, Se powder and $NaBH_4$. | - | 135 | 37 | [76], 2015 |
| Ultra-thin Fe–Ni–S | 0.5 M $H_2SO_4$ | Topotactic conversion from FeNi layered double hydroxide (LDH) | 2 nm | 105–117 | 40–48 | [77], 2015 |
| $NiCo_2S_4$ | 1.0 M KOH | Sulfidation of NiCo-LDH | 10-15 nm | 65 | 84.5 | [78], 2016 |
| Mn-doped $CoSe_2$ | 0.5 M $H_2SO_4$ | Conventional liquid exfoliation of Mn-incorporated $CoSe_2$/DETA | 1.2 nm | 195 | 36 | [66], 2016 |
| Se-enriched $NiSe_2$ | $H_2SO_4$ pH~0.67 | Vapor selenization of $Ni(OH)_2$ | - | 117 | 32 | [79], 2016 |
| $Co_3S_4$ | 1.0 M KOH | Plasma-assisted conversion of $Co_3S_4$/triethylenetetramine | 1 nm | 63 | 58 | [80], 2018 |
| NiSe | 1.0 M NaOH | Topotactic transformation strategy with $Ni(OH)_2$/NaHSe | 1.25 nm | 177 | 58.2 | [81], 2018 |
| $Ni_3N$ | 0.5 M $H_2SO_4$ | Simple sintering process with $Ni(CH_3CO_2)_2$. $4H_2O$ and urea | - | 100 (100 mA $cm^{-2}$) | 59.79 | [82], 2016 |
| $Mo_5N_6$ | 1 M KOH | Ni-induced salt-templated method | 3 nm | 94 | 66 | [83], 2018 |
| CoP | 0.5 M $H_2SO_4$ | Phosphidation of α-$Co(OH)_2$ | - | 90 | 43 | [84], 2014 |
| $Ni_5P_4$–$Ni_2P$ | 0.5 M $H_2SO_4$ | Phosphorization of commercially available nickel foam | - | 120 | 79.1 | [85], 2015 |
| Mo–W–P | 0.5 M $H_2SO_4$ | Phosphidation of molybdenum tungsten oxide | - | 93 (20 mA $cm^{-2}$) | 52 | [86], 2016 |
| MoP | 0.5 M $H_2SO_4$ | Phosphidation of $MoS_2$ | - | 124 | 58 | [87], 2016 |
| FeCoP | 1 M KOH | Phosphidation of CoFe-LDH | 1.1 nm | 188 (100 mA $cm^{-2}$) | 76 | [88], 2017 |
| CoP | 0.5 M $H_2SO_4$ | Phosphidation of 2D $Co_3O_4$ | 1.1 nm | 56 | 44 | [89], 2017 |
| CoP | 0.5 M $H_2SO_4$, 1 M KOH, and 1 M PBS | Phosphatization of 2D $Co_3O_4$ aerogel with $NaH_2PO_2 \cdot 2H_2O$ | <1.5 nm | 113 ($H_2SO_4$) 154 (KOH) 161 (PBS) | 67($H_2SO_4$) 72(KOH) 81(PBS) | [90], 2018 |
| $Co_2P$ | 0.5 M $H_2SO_4$ | Salt-templating method with $Co(NO_3)_2 \cdot 6H_2O$ and $(NH_4)_2HPO_4$ | 4 nm | 41 | 35 | [91], 2018 |
| FeP | 0.5 M $H_2SO_4$ | Phosphidation of γ-$Fe_2O_3$ with $NaH_2PO_2$ at 320 °C | 0.7 nm | 95 | 41 | [92], 2019 |
| Mo-Doped CoP | 1 M KOH | Phosphidation of Mo-Co(OH)F with $NaH_2PO_2$ at 300 °C | 10-15 nm | 49 | 80 | [93], 2019 |
| N,P-graphene[a] | 0.5M $H_2SO_4$ | porous-metal-based chemical vapor deposition | - | 344 | 118 | [94],2019 |
| S-doped $C_3N_4$[a] | 0.5M $H_2SO_4$ | Polycondensation of trithiocyanuric acid, | 0.325nm | 186 | 84 | [95],2017 |

| | | | | | | |
|---|---|---|---|---|---|---|
| S-vacancies and Edge-rich $MoS_2$[a] | 0.5M $H_2SO_4$ | Lithiation, desulfurization, and exfoliation | ~1.5nm | 153 | 43 | [96],2016 |
| $WSe_2$[a] | 0.5 M $H_2SO_4$ | Mechanically exfoliation | ~1 nm | 245 | 76 | [97]2016 |
| Edge-rich $MoS_2/Ni(OH)_2$ hybrid[a] | 1 M KOH | Liquid exfoliation and cathodic electrodeposition process | - | 57 | 30 | [98]2020 |

[a] Representative 2D layered materials for comparison

To improve the kinetics of HER on metal surface, great efforts have been focusing on metal alloying. Well-defined alloys often exhibit better catalytic properties than their monometallic counterparts due to the synergistic catalytic effect[72] and the evolving of surface electronic state.[73] In metal alloy, mutual pairing and sharing of d-orbital electron could tune electronic configurations suitable for proton adherence and transference.[99] Metikoš-Hukovic *et al*. reported that the Ni-Zr alloy exhibited a rapid increase of DOS of the Ni 3d orbitals at the Fermi level, which consequently led to a weaker bond of M–$H_{ads}$ and a higher activity for HER.[100] The synergistic effect of metal alloy and 2D geometry could further enhance the electrocatalytic activity. 2D materials from metal alloys of Pt-Cu[72], Ni-Mo[73], Pt-Ag-Co[74], Pd-Cu[75] and Ru-Pd-Ni[101] have been studied for HER performance. Zhao *et al.* found out 2D Pd-Cu alloy with a thickness of 1.8 nm only needed an overpotential of 106 mV to achieve an HER current density of 10 mA $cm^{-2}$ in alkaline media; while 2D Pd needed an overpotential of 235 mV to reach the same current density.[75] Zhang *et al*. reported electrocatalytic HER by the 2D non-noble Ni–Mo alloy synthesized by *in situ* topotactic reduction of $NiMoO_4$ precursor.[73] Introducing Mo into Ni could modify the electron DOS of the d orbitals and thus change $\Delta G_H$ on the metal surface.[102] 2D Ni-Mo with a thickness of 2.0–2.1 nm showed an overpotential of 35 mV at a current density of 10 mA $cm^{-2}$ (**Figure 5d**), along with a Tafel slope of 45 mV $dec^{-1}$, demonstrating a comparable catalytic activity to commercial Pt/C catalyst. Besides, 2D Ni-Mo showed a faster mass transfer behavior at high current density as

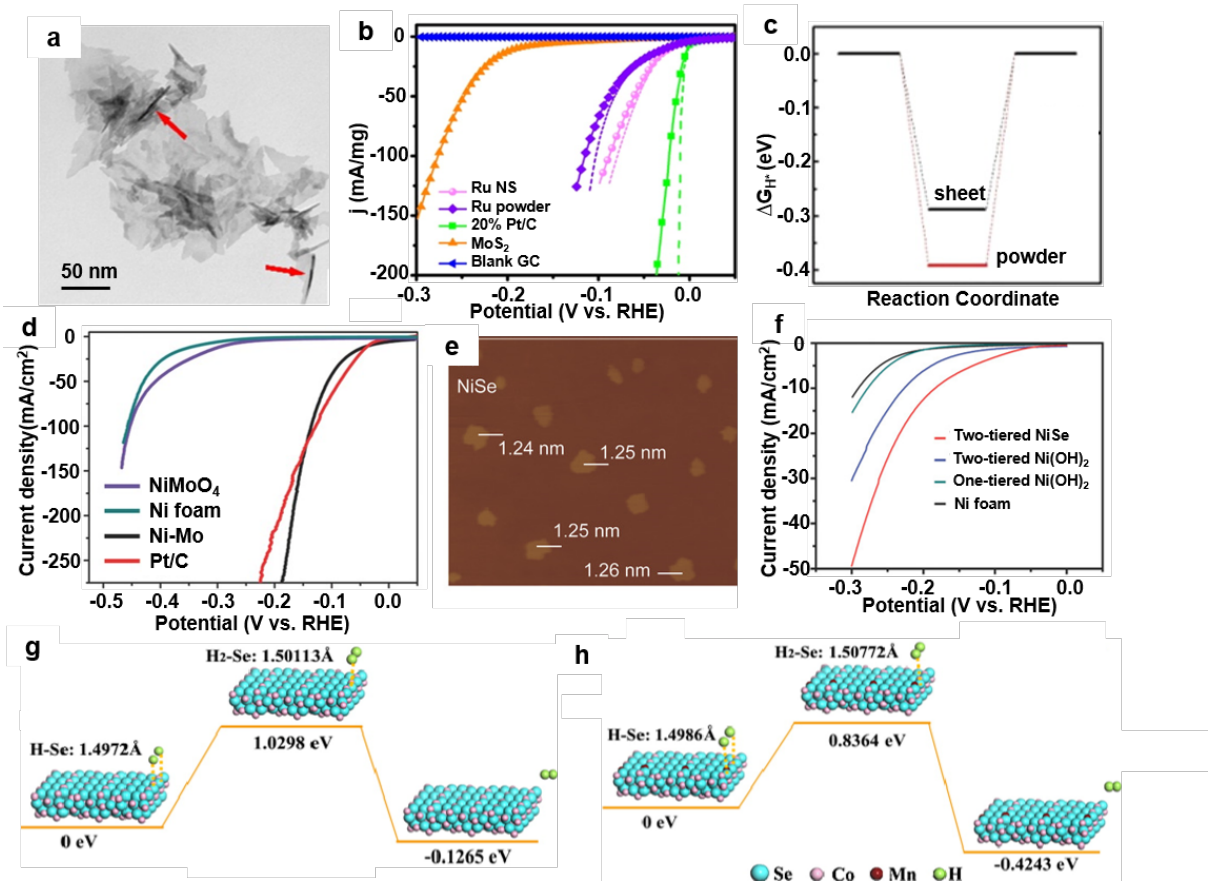


**Figure 5.** Different types of 2D non-layered materials for HER. (**a**) TEM of as synthesized 2D Ru. (**b**) LSV of 2D Ru in HER in 0.5 M $H_2SO_4$ electrolyte with pH = 0. (**c**) HER free energy diagram calculated at the equilibrium potential for 2D Ru and powder surfaces. [70]Reproduced with permission from © Copyright 2016 American Chemical Society. (**d**) Polarization curves of 2D Ni-Mo (0.8 mg $cm^{-2}$), Pt/C (1.6 mg $cm^{-2}$) powder, $NiMoO_4$ precursor, and Ni foam in 1 M KOH. [73]Reproduced with permission from © 2017 Wiley-VCH Verlag GmbH & Co. KGaA, Weinheim. (**e**) AFM images of 2D NiSe. (**f**) HER LSV curves of two-tiered NiSe, two-tiered $Ni(OH)_2$, one-tiered $Ni(OH)_2$ 2D materials, and bare Ni foam. [81]Reproduced with permission from © 2018 Wiley-VCH Verlag GmbH & Co. KGaA, Weinheim. (**g, h**) The kinetic energy barrier profiles of the hydrogen evolution reaction on the edge sites of virgin $CoSe_2$ and Mn doped 2D $CoSe_2$, respectively. [66]Reproduced with permission from © Copyright 2016 American Chemical Society.

compared to Pt/C catalyst. These impressive initial successes argued that 2D metal alloys would be a promising new solution for developing low cost and high efficient non-noble metal HER catalysts.

### 3.2. Transition metal chalcogenides

Transition metal chalcogenides (TMC) have been studied as HER catalysts because of the predicated low $\Delta G_H$[103] as well as their low cost and high stability. 2D non-layered TMCs were typically prepared by topotactic conversion of layered precursors. 2D TMCs including $NiCo_2S_4$,[78] $NiSe_2$ [76 79], NiSe[81], NiS[77], $Ni_{1-x}Fe_xPS_3$,[104], $CoSe_2$[66], and $Co_3S_4$[80] have been synthesized and studied for HER applications. Wu *et al*. made ~1.25 nm 2D NiSe from 2D $Ni(OH)_2$ precursors (**Figure 5e**) and studied their full water electrolysis behavior.[81] 2D NiSe displayed an improved HER performance with a lower onset overpotential (177 mV at 10 mA $cm^{-2}$) and a smaller Tafel slope (58.2 mV $dec^{-1}$) compared to those of layered $Ni(OH)_2$ (**Figure 5f**). The improvement was attributed to the largely exposed catalytically active Se sites on the 2D structure, as the free energy for hydrogen adsorption was much lower at the Se sites (0.13 eV) than the Ni sites (0.87 eV). By creating Se-enriched 2D $NiSe_2$, the overpotential was further lowered to 117 mV at 10 $mAcm^{-2}$ with a smaller Tafel slope of 32 mV $dec^{-1}$.[79] Similar high HER performance was also obtained from iron-nickel sulfide 2D materials synthesized by topotactic conversion.[77] Because $H_2$ prefers to form at the Fe sites rather than the Ni sites, Fe-incorporation could change the catalytically active center, and thus facilitate the HER process. DFT simulation further confirmed the lower energy barrier for $H^+$ adsorption and higher exothermicity for $H_2$ formation on iron-nickel sulfide 2D materials when Fe was presented, which was believed to be the main reason for the improved HER performance.

In addition to material selection, point defects were often manipulated to further improve the catalytic performance of TMCs, including extrinsic dopant and intrinsic vacancy control. As discussed in section 2.3, incorporating Mn ions in the $CoSe_2$ crystal lattice could induce subtle distortion of the atomic arrangement, and thus bring additional exposed active edge sites. Moreover, the electronic structure of 2D $CoSe_2$ could be adjusted by Mn doping, which lowered the energy barriers of H–H bond formation and final $H_2$ release (**Figure 5g-h**). As a result, Mn-doped 2D $CoSe_2$ displayed a much better HER catalytic activity than undoped $CoSe_2$, including a lower overpotential of 174 mV, a smaller Tafel slope of 36 mV $dec^{-1}$, and a larger exchange current density of 68.3 μA $cm^{-2}$.[66] Vacancies, as a common intrinsic point defect, could also effectively modulate the HER performance of 2D materials. As an example, abundant sulfur-vacancies confined in porous 2D $Co_3S_4$ were developed for HER catalysis.[80] The S-deficient 2D $Co_3S_4$ showed an extremely large mass activity of 1056.6 A $g^{-1}$ at an overpotential of 200 mV, which was superior to commercial Pt/C catalysts, and over 14 times and 107 times higher than the value of 2D $Co_3S_4$ and $Co_3S_4$ nanoparticles, respectively. Through electrochemical capacitance measurements, the amount of catalytically active sites was found significantly increased by introducing S vacancies to 2D $Co_3S_4$. DFT calculation revealed that $Co_3S_4$ with S vacancies had a larger adsorption energy of $H_2O$ molecules and a relatively lower water-dissociation energy barrier, which could help reaching the intermediate catalyst-H stage and accelerate the kinetics for alkaline HER. Furthermore, the S vacancies could bring more electrons to the occupied states in the range from -0.26 eV to the Fermi level, indicating enhanced electrical conductivity.

### 3.3. Metal nitrides

Metal nitrides are attractive for electrocatalytic HER mostly due to their metallic behavior, which can effectively facilitate electron transport during the HER process. Furthermore, the unique electronic structure of transition metal nitrides can provide suitable adsorption of $H^+$ on the crystal surfaces.[105] For example, Guo *et al*.[82] synthesized atomically thin metallic 2D $Ni_3N$ by a simple annealing approach, which displayed excellent HER performance in the whole pH range (1-14) close to that of commercial Pt/C electrodes. It was found that the Ni atoms accompanied by surrounding N atoms on the N–Ni surface acted as the most active HER sites ($\Delta G_H$ = 0.065 eV). Thus, together with its good electrical conductivity, the 2D $Ni_3N$ exhibited excellent catalytic kinetics for HER as well as a remarkable durability (negligible loss for over 5000 cycles). Furthermore, holey structure has been introduced to 2D nitrides materials to facilitate the diffusion of intermediates and gases during HER and to expose a larger number of surface catalytically active atoms in the hole area. Metallic 2D holey $Ni_3Fe$ nitride with 0.6-0.8 nm in thickness was synthesized by nitridation treatment of corresponding hydroxide precursors. They demonstrated excellent electrocatalytic performance for both of HER and OER with a kinetic rate higher than that of Pt/C catalyst.[106] However, due to the low valence state of the metal atoms, many metal nitrides could be oxidized during the electrocatalytic processes, which led to relatively low stability. To solve this problem, Jin *et al*. synthesized nitrogen-rich 2D metal nitrides $Mo_5N_6$ with a higher Mo valence state, leading to better corrosion resistance toward HER.[83] Due to the incorporation of additional nitrogen atoms in the lattice, $Mo_5N_6$ showed Pt-like electronic structure. As a result, $Mo_5N_6$ exhibited an outstanding HER performance within the entire PH range. Furthermore, the HER activity with natural seawater showed a highly stable catalytic current over 100 hours, which outperformed commercial Pt/C and other metal nitride electrocatalysts. Nevertheless, although high HER performance has been demonstrated with 2D metal nitrides, their poor stability in aqueous electrolyte still largely limits their catalytic applications, particularly under high or low pH conditions.

### 3.4. Transition metal phosphides

Non-layered 2D transition metal phosphides are emerging as another class of attractive electrocatalysts for HER in recent years due to their metalloid characteristics and good electrical conductivity. In particular, cobalt phosphide (CoP) has attracted widespread attention owing to low cost, high catalytic activity, and great operational stability. Pu et al. developed a facile strategy to synthesizing 2D CoP arrays on a Ti plate as a highly-active HER catalyst via low temperature phosphidation of α-$Co(OH)_2$/Ti precursor.[84] The CoP/Ti electrode showed a high HER activity in acidic solutions with a low overpotential of 90 and 146 mV at 10 and 100 mA $cm^{-2}$, respectively. CoP/Ti exhibited a Tafel slope of 43 mV $dec^{-1}$ in the region of η = 40 - 120 mV. Furthermore, CoP/Ti electrode exhibited a good stability (10000 s) and nearly 100% Faradaic efficiency for $H_2$ evolution. Porous 2D CoP was also created with exposed reactive (200) facet *via* phosphidation of $Co_3O_4$ precursors.[89] The as-synthesized 2D CoP showed outstanding HER performance in

acidic solutions with an even lower overpotential of 56 and 131 mV from a few other metal-doped 2D CoP (Metal = Fe, Ni, and Mg).[88]

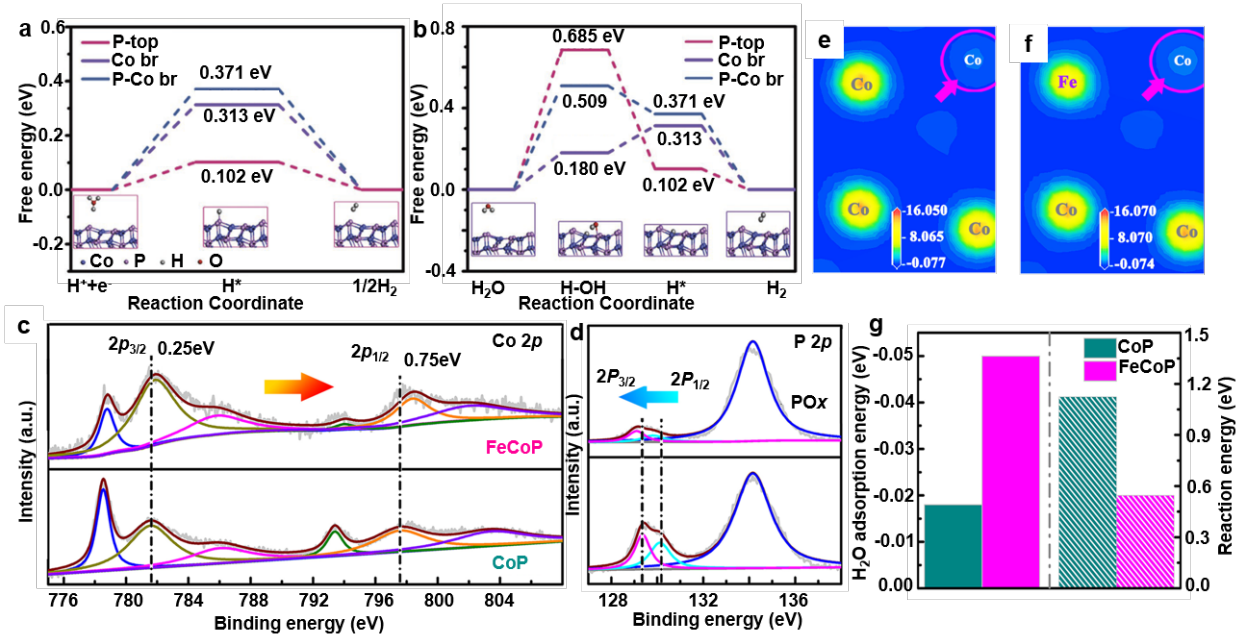


**Figure 6**. 2D transition metal phosphides for HER (**a**) The corresponding free energy diagram for HER of CoP (011) in P-top, Co bridge, and P–Co bridge sites under the acid condition. Top inset is the simulated (011) facets of CoP: Co atoms: blue, P atoms: purple. (**b**) The corresponding free energy diagram for HER of CoP (011) in P-top, Co bridge, and P–Co bridge under the alkaline condition. [90]Reproduced with permission from © 2018 Wiley-VCH Verlag GmbH & Co. KGaA, Weinheim. (**c**) Co 2p and (**d**) P 2p orbital XPS spectra of FeCoP; the charge density distributions of (**e**) FeCoP and (**f**) CoP; (**g**) adsorption energies of $H_2O$ molecule, and the hydrogen dissociation energy on the surface of CoP and FeCoP. [88]Reproduced with permission from © 2017 Elsevier Ltd.

at 10 and 100 mA $cm^2$, respectively; while the Tafel slope (44 mV $dec^{-1}$) was almost the same as solid 2D CoP discussed above. The stability was significantly improved to over 20 hours. The extremely small thickness and porous structure rendered an extraordinarily high mass activity of 151 A $g^{-1}$ at an overpotential of 100 mV, which was ~80 times higher than that of CoP nanoparticles. To achieve a scalable application of 2D CoP electrocatalysts, Li *et al*. reported an ice-templating strategy to synthesizing aerogels of 2D CoP.[90] The highly porous aerogel structure brought advantages of short electron transfer distance and abundant exposed active sites, resulting in excellent electrocatalytic HER performance. The current density experienced a negligible loss at all pH values after 70,000 s, evidencing its remarkable stability. DFT calculations revealed that that P-top and Co bridge on the CoP (011) facet were the active sites for HER in acid and alkaline solutions, respectively (**Figure 6a, b**). Because these active sites were always located on a defined crystal facet, single crystalline 2D structures could enable the exposure of the most active facets for HER. Li *et al*. presented the synthesis of various single crystalline 2D metal phosphides with well-defined exposed crystal facets by a salt-templating method. The as-synthesized 2D $Co_2P$ with exposed (130) facets exhibited the greatest HER catalytic activity with an overpotential of 41 mV at 10 mA $cm^{-2}$ and a Tafel slope of 35 mV $dec^{-1}$ in 0.5 M $H_2SO_4$ solution as well as good stability.[91]

In addition to material selection, element doping can further improve the catalytic performance by tuning the electronic structure. Similar to the TMC systems, Mo doping in 2D CoP induced a significant improvement in the HER activity with low overpotentials of 49 and 120 mV at 10 and 100 mA $cm^{-2}$, respectively.[93] Similar outstanding electrocatalytic HER activities were also demonstrated Compared to the undoped one, Fe-doped 2D CoP exhibited superior HER activity with a lower onset potential (~ 45 mV), an overpotential of 188 mV at 100 mA $cm^{-2}$, and a smaller Tafel slope of 76 mV $dec^{-1}$. XPS characterization discovered that the Co 2p and P 2p in Fe-CoP were positively- and negatively-shifted compared to pristine CoP (**Figure 6c, d**), suggesting that Fe doping could enhance the electron interaction between Co and P. The adsorption behavior of $H_2O$ on electrocatalyst surface is an important factor for HER in basic electrolyte. Theoretical study revealed that the electronic structure of Co was modulated by Fe incorporation (**Figure 6e, f**), and the adsorption energy of $H_2O$ molecule on Fe-CoP (−0.05 eV) was much lower than that on CoP (−0.018 eV) (**Figure 6g**), implying a more thermodynamically favorable $H_2O$ adsorption on Fe-CoP accounting for the largely enhanced HER activity.

In addition to cobalt phosphide, other 2D transition-metal phosphides also displayed comparable HER activities due to their similar crystal structure and electrochemical properties, which included $NiP_2$,[107] $Ni_5P_4$-$Ni_2P$[85], MoP on carbon cloth[87], porous Mo–W–P hybrids[86], and phosphate-doped FeP[92]. Nevertheless, stability is also a big concern for these group of materials, because surface reactions and reconstructions, particularly oxidation, reduction and amorphization would easily occur during the electrochemical processes.[108]

## 4. Oxygen evolution reaction

In electrochemical water splitting, the efficiency is largely limited by the OER half reaction because of its sluggish reaction kinetics related to a complex four-electron redox process. During a typical OER process, $H_2O$ first adsorbs at the active sites (e.g. O-vacancies)

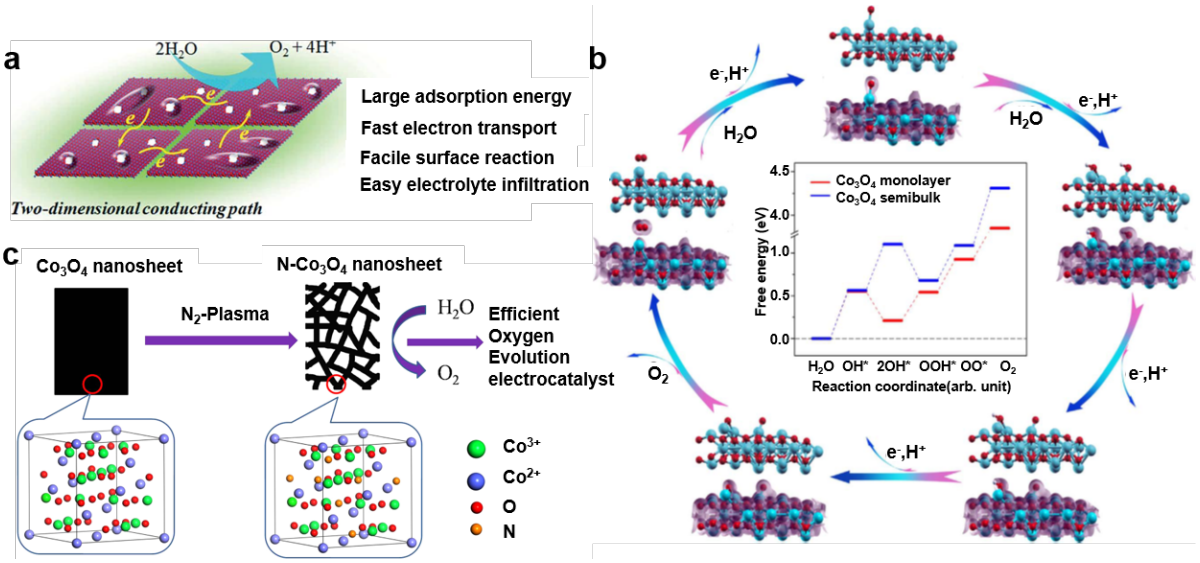


**Figure 7.** Advantages of the 2D structure for the OER. (**a**) 2D conducting path and advantages of atomically thin $Co_3O_4$ sheets for the OER. [60]Reproduced with permission from © The Royal Society of Chemistry 2014. (**b**) DFT calculations on screening of electrocatalytic activities on (111) facets of $Co_3O_4$ monolayer and semibulk. Outer ring: schematic illustration of the OER process and the valence density isosurface for each reactant along the pathway. Center: the calculated free energies of the $Co_3O_4$ monolayer and semibulk. [111]Reproduced with permission from © 2016 Elsevier Ltd. (**c**) Schematic illustration of the preparation of the N-doped 2D $Co_3O_4$ for efficient OER. [113]Reproduced with permission from © IOP Publishing Ltd 2017.

on the catalyst surface.[109] Upon receiving a hole, one H-O bond in the $H_2O$ molecule is broken and oxidized to form OH*, which is further oxidized yielding an O*. The O* then reacts with another $H_2O$ molecule forming an OOH* and eventually evolved into $O_2$ through a deprotonation process.[53] In this process, the active sites are essential in controlling the overall reaction rate. Increasing the number of active sites and improving their reactivity are two commonly used strategies to raise the OER electrocatalytic performance. Compared to other geometries, 2D non-layered materials offer unique synergistic advantages for OERs, including large adsorption energy, fast electron transport, facile surface reaction, and easy electrolyte infiltration (**Figure 7a**).[60, 110]

DFT calculations comparing the catalytic activity of the (111) facet of monolayer and semibulk $Co_3O_4$ depicted the advantages of 2D morphology. [111] **Figure 7b** illustrates the OER pathway on $Co_3O_4$ (111) surface. The center chart presents the calculated reaction energies of each intermediate step for the two morphologies. According to the energy variations along the reaction pathways, the biggest difference lies in the adsorption of second OH*, where $Co_3O_4$ monolayer requires much less energy because the interaction between two adsorbed OH* is much stronger. Furthermore, the following reaction steps on monolayer also require less energy than those on semibulk. Together they bring in a much lower overall OER energy barrier for $Co_3O_4$ monolayer (3.85 eV) compared to that of semibulk (4.31 eV). This calculation suggested that it is the structural distortion in the monolayer morphology that reduces the energy barrier and largely increases the activity of OER catalysis. Besides, similar to HER, the 2D non-layered geometry also promotes oxygen reactivity by increasing the number of catalytic active sites and improving the electrical conductivity, owing to their extremely large number of unsaturated surface atoms and the structural disorders associated with their atomic thickness. Doping the 2D lattices are also regarded as an effective strategy to improve the 2D conductivity and to introduce more oxygen vacancies that promote OER activity (**Figure 7c**).[112, 113] Nanoscale pores, which often formed in solution-based synthesis processes, were found beneficial for catalysis as they promote electrolyte infiltration.

2D non-layered materials always show superior OER activity over pure layered materials, owing to the extremely large number of unsaturated surface atoms and the lattice distortion. For example, 2D non-layered $CoSe_2$ is a promising candidate for high OER performance with an $\eta_{10}$ of 0.32 V, while layered $MoS_2$ for OER is limited in alkaline conditions. Layered double hydroxides (LDHs) are promising candidates for OER because of their natural abundance and lower costs. However, the lack of active sites and poor electrical conductivity in LDHs make them unsuitable for electrocatalysis, and many efforts have been devoted to increase the active edge sites for higher OER performance in recent years. Pure graphene- and g-$C_3N_4$-based layered materials also showed poor intrinsic OER performance. It was found that spin redistribution induced by heteroatom-doping in the graphene matrix can improve the OER catalytic activities. Black phosphorus is another representative 2D layered material that has attracted increasing attention because of its lone-pairs of electrons on the surface, and anisotropic electrical properties. However, similar to LDHs, the OER performance of bulk BP is also limited by insufficient active sites.

A chronological summary of different 2D non-layered materials, and their characteristic parameters reported of OER **in Table 2**. Different from HER, 2D non-layered OER catalysts are mostly oxides due to the requirement of $H_2O$ adsorption. Our discussion will focus on these groups of materials and a few other alternatives that showed good $H_2O$ adsorption capability.

### 4.1. Metal oxides

Metal oxides are most commonly used OER catalysts due to their good stability and abundant oxygen vacancies. In recent years, many

earth-rich transition metal oxides (TMOs) like CoO[53], $Co_3O_4$[111], CuO, [110] NiO[109, 114], $La_2O_3$[46] and $NiCo_2O_4$[115] have been intensively studied as OER catalysts to replace noble metal oxides such as $RuO_2$ and $IrO_2$. Among them, $Co_3O_4$ distinguished due to its high performance and good sustainability (*e.g.* environment friendliness and rich in reserve). Li *et al.* synthesized 2D $Co_3O_4$ through a facile and scalable surfactant-free cyanogel-$NaBH_4$ method.[116] The 2D $Co_3O_4$ exhibited a uniform thickness of ~1.5 nm and rich of nanoscale pores (**Figure 8a**). The pores were formed during the assembly of crystal nuclei. As shown in **Figure 8b**, when applied to OER, the 2D $Co_3O_4$ showed an onset potential of 101 mV, which was lower than that of commercial $RuO_2$ (408 mV). The overpotential of 2D $Co_3O_4$ at the current density of 10 mA $cm^{-2}$ was also ~100 mV lower than that of $RuO_2$. This performance enhancement was owing to the high surface area and abundant defect sites at the pore edges favoring mass transport.

To improve the O-vacancy concentration, Bao *et al*. created bimetallic oxide ($NiCo_2O_4$) in the 2D morphology (**Figure 8c**).[115] The as-prepared 2D $NiCo_2O_4$ was 1.6 nm in thickness (2 unit cells). Rich oxygen vacancies were induced as a result of calcination in an oxygen deficient atmosphere, which improved the reactivity of active sites and reduced the $H_2O$ adsorption energy. The ultrathin thickness improved the amount of active sites and thus facilitated the surface reactions. The roughness factor ($R_f$) calculated from CVs of 2D $NiCo_2O_4$ with rich oxygen vacancies (NiCo-r) and poor oxygen

In addition to the capability of serving as descend HER catalysis, some TMCs also acted very well in OER processes. Nevertheless, the fundamental mechanism of TMCs for OER has not been fully understood thus far.[117, 118] It was suggested that TMCs could be oxidized to corresponding metal oxides/hydroxides on the surface in a strongly oxidative environments of OER. The fresh surfaces were usually more catalytically active comparing to metal oxides hydroxides synthesized directly. Therefore, TMCs like $Co_3S_4$, $Co_9S_8$, and $CuCo_2S_4$, stand as a unique group of materials that can be used for catalyzing full electrocatalytic water splitting reactions.[119-122] In a representative example, 2D $CoS_x$ synthesized by post-sulfurizing $Co(OH)_2$ were used for OER, HER, and overall water splitting.[120] The as-synthesized 2D materials had a thickness of less than 1 nm and a size of ~100 nm (**Figure 8e**). The large number of exposed surface atoms contributed high electrocatalytic activity, and the ultrathin and mesoporous structures benefited the mass and charge transfer through the 2D structure. The Nyquist plots from electrochemical impedance spectroscopy (EIS) revealed that the charge-transfer resistances of 2D $CoS_x$ and $Co_9S_8$ (annealed $CoS_x$) were much lower than that of commercial $RuO_2$ (**Figure 8f**). It evidenced the faster faradaic process and higher electric conductivity at the electrode-electrolyte interface of 2D $CoS_x$ and $Co_9S_8$. 2D $FeS_2/CoS_2$ mixture with thicknesses of 1.6 to 2.8 nm were prepared by annealing $CoFe_2O_4$ nanoparticles with sublimed sulfur in a $N_2$ atmosphere (**Figure 8g**).[123]

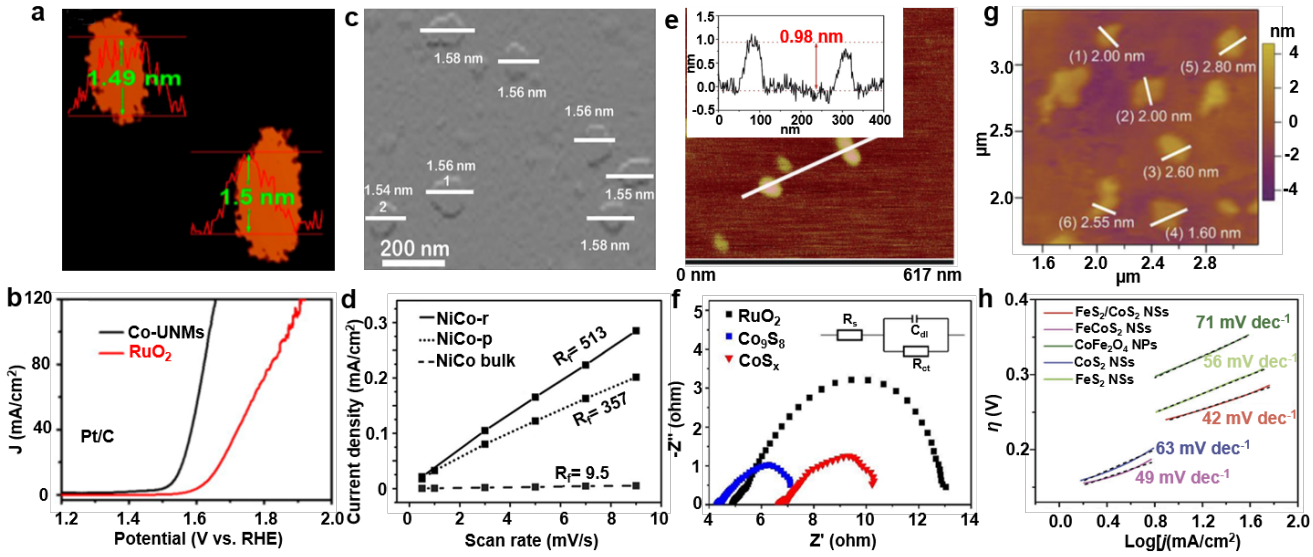


**Figure 8**. Different types of 2D non-layered material for OER. (**a**) AFM image of 2D $Co_3O_4$ with corresponding height profiles. (**b**) The iR-corrected LSV curves of 2D $Co_3O_4$ and commercial $RuO_2$ in $O_2$-saturated 1 M KOH electrolyte at a scan rate of 5 mV $s^{-1}$. [116]Reproduced with permission from © 2018 American Chemical Society. (**c**) AFM image and height profiles of 2D $NiCo_2O_4$. (**d**) The roughness factor (Rf) values of 2D $NiCo_2O_4$ with rich oxygen vacancies (NiCo-r) and poor oxygen vacancies (NiCo-p), and a bulk sample, which are measured at 0.24 V in 1 M KOH solution at scan rates from 0.5 to 9 mV $s^{-1}$ of the corresponding CVs. [115]Reproduced with permission from © 2015 Wiley-VCH Verlag GmbH & Co. KGaA, Weinheim. (**e**) AFM image and height profiles of 2D $CoS_x$. (**f**) Nyquist plots of 2D $CoS_x$ and $Co_9S_8$ (annealed $CoS_x$), and commercial $RuO_2$ in the frequency range of 100 kHz to 0.01 Hz for η = 365 mV. [120]Reproduced with permission from © The Royal Society of Chemistry 2018. (**g**) AFM image of 2D $FeS_2/CoS_2$ with corresponding height profiles. (**h**) Tafel plots of different catalysts at the scan rate of 2 mV $s^{-1}$ in 1 M KOH electrolyte. [123]Reproduced with permission from © 2018 Wiley-VCH Verlag GmbH & Co. KGaA, Weinheim.

vacancies (NiCo-p) were both 40-50 times larger than that of the bulk sample (**Figure 8d**). The higher $R_f$ value represented more surface active sites, confirming the advantage of 2D morphology for enhancing the electrocatalytic performance.

### 4.2. Transition Metal chalcogenides

As shown in **Figure 8h**, the Tafel slope of 2D $FeS_2/CoS_2$ (42 mV·$dec^{-1}$) was lower than $CoFe_2O_4$ nanoparticles and other catalysts, demonstrating a higher OER reaction rate. The superb OER performance was attributed to the large specific surface area of the 2D structure and rich interface defects that benefit the adsorption and activation of reactants. The superior catalytic performance for both OER and HER suggested that 2D transition metal chalcogenides

REVIEW

**Table 2.** Summary of 2D non-layered materials reported for OER electrocatalysts.

| Catalyst | Synthetic method (precursor) | Thickness | Electrolyte | Electrochemical performance | Refs., year |
|---|---|---|---|---|---|
| CoO | Ionic layer epitaxy method ($Co(NO_3)_2$ $6H_2O$ and hexamethylenetetramine) | 2.8 nm | 1 M NaOH | Overpotential of 560 mV at 10 mA·cm$^{-2}$; Tafel slope of~85 mV·dec$^{-1}$ (*vs*. RHE) | [53], 2017 |
| $Co_3O_4$ | Fast-heating strategy (CoO) | 0.43 nm | 1 M KOH | Electrocatalytic current of 341.7 mA·cm$^{-2}$ at 1.0 V *vs*. Ag/AgCl, | [60], 2014 |
| $Co_3O_4$ | One-step approach ($CoCl_2/K_3Co(CN)_6$) | 1.5 nm | 1 M KOH | Overpotential of 307 mV at 10 mA·cm$^{-2}$; Tafel slope of 76 mV·dec$^{-1}$ (*vs*. RHE) | [116], 2018 |
| $Co_3O_4$ | Self-assembly approach (Polyethylene oxidepolypropylene oxide-polyethylene oxide) | 1.8 nm | 0.1 M KOH | Onset potential of 0.617 V *vs*. Hg/HgO; Current density of 12.26 mA·cm$^{-2}$ at 0.8 V *vs*. Hg/HgO | [111], 2016 |
| $Co_3O_4$ | Hydrothermal method ($NaBH_4$) | 11 nm | 1 M KOH | Overpotential of 318 mV at 10 mA·cm$^{-2}$ (*vs*. RHE); Overpotential of 436 mV, the current density can be reached up to as high as 800 mA cm$^{-2}$ | [124]2018 |
| $La_2O_3$ | Ionic layer epitaxy method ($La(NO_3)_3$, hexamethylenetetramine, oleylamine) | 2.27 nm | 1 M NaOH | Overpotential of 310 mV at 10 mA·cm$^{-2}$; Tafel slope of 43.1 mV·dec$^{-1}$ (*vs*. RHE) | [46], 2019 |
| N-doped $Co_3O_4$ | $N_2$ plasma ($Co_3O_4$) | - | 0.1 M KOH | Overpotential of 310 mV at 10 mA·cm$^{-2}$; Tafel slope of 59 mV·dec$^{-1}$ (*vs*. RHE) | [113], 2017 |
| CuO | Chemical bath deposition method ($CuSO_4$, $NH_4OH$) | 10-15 nm | 1 M KOH | Overpotential of 350 mV at 10 mA cm$^{-2}$; Tafel slope of 59 mV dec$^{-1}$ (*vs*. RHE) | [110], 2017 |
| NiTi oxide | Reverse microemulsion method ($TiO_2$, NiTi-LDH) | 1 nm | 1 M KOH | Overpotential of 320 mV at 10 mA·cm$^{-2}$; Tafel slope of 52 mV·dec$^{-1}$ (*vs*. RHE) | [109], 2016 |
| $NiCo_2O_4$ | Topochemical method (NiCo hydroxies) | 1.56 nm | 1 M KOH | Current density of 285 mA ·cm$^{-2}$ at 0.8V (vs. RHE); Overpotential of 0.32V (*vs*. RHE) | [115], 2015 |
| $Fe_1Co_1$-oxide | Solution reduction method ($Fe(NO_3)_3$, $Co(NO_3)_2$, CTAB) | 1.2 nm | 0.1 M KOH | Overpotential of 308 mV at 10 mA·cm$^{-2}$; Tafel slope of 36.8 mV·dec$^{-1}$ (*vs*. RHE) | [125], 2017 |
| $Fe_1Co_1O_x$ | Hydrothermal and hydrogenation method ($Fe(NO_3)_3$, $Co(NO_3)_2$, and CTAB) | 1.2 nm | 1 M KOH | Overpotential of 225 mV at 10 mA·cm$^{-2}$; Tafel slope of 36 mV·dec$^{-1}$ (*vs*. RHE) | [126], 2018 |
| $Co_3S_4$ | Ultrasound exfoliation treatment $Co_3S_4$/triethylenetetramine | 1.0 nm | Neutral solution | Overpotential of 0.7 V at 3.97 mA·cm$^{-2}$; Overpotential at 0.31V (*vs*. RHE) | [121], 2015 |
| $Co_9S_8$ | Polyol refluxing, sulfurization and calcination process (graphene oxides or $Co(Ac)_2$) | 3~4 nm | 1 M KOH | Overpotential of 266 mV at 10 mA·cm$^{-2}$; Tafel slope of 75.5 mV·dec$^{-1}$ (*vs*. RHE) | [119], 2019 |
| $Co_9S_8$ | Microwave-assisted liquid-phase growth ($Co(OH)_2$) | 0.98 nm | 1 M KOH | Overpotential of 288 mV at 10 mA·cm$^{-2}$ (*vs*. RHE) | [120], 2018 |
| $CuCo_2S_4$ | Metal activity and structure-directed one-pot sulfurization strategy (Cu and Co ions) | 10-13 nm | 0.1 M KOH | Overpotential of 337 mV at 10 mA·cm$^{-2}$ (*vs*. RHE) | [122], 2016 |
| $FeS_2/CoS_2$ | Sulfurization and calcination method ($CoFe_2O_4$) | 1.6-2.8 nm | 1 M KOH | Overpotential of 302 mV at 100 mA·cm$^{-2}$; Tafel slope of 42 mV·dec$^{-1}$ (*vs*. RHE) | [123], 2018 |
| Co-Based MOFs | Surfactant-assisted hydrothermal method ($Co^{2+}$ and benzenedicarboxylic acid (BDC)) | 2 nm | 1 M KOH | Overpotential of 263 mV at 10 mA·cm$^{-2}$; Tafel slope of 74 mV·dec$^{-1}$ (*vs*. RHE) | [127], 2018 |
| NiCo bimetal-MOFs | Ultrasonic method ($Ni^{2+}$, $Co^{2+}$ and BDC) | 3.1 nm | 1 M KOH | Overpotential of 189 mV at 10 mA·cm$^{-2}$; Onset potential of 1.39 V (*vs*. RHE) | [128], 2016 |
| CoCo LDH[a] | Exfoliation method | 1 layer | 1 M KOH | Overpotential of 319 mV at 10 mA·cm$^{-2}$; Tafel slope of 42 mV·dec$^{-1}$ (*vs*. RHE) | [129], 2019 |
| $MoS_2$[a] | Chemical stripping | 1.5 nm | 0.5 M $H_2SO_4$ | Overpotential of 450 mV at 10 mA·cm$^{-2}$; Tafel slope of 322 mV·dec$^{-1}$ (*vs*. RHE) | [130], 2016 |
| g-$C_3N_4$[a] | Ultrasonic exfoliation | 1.1 nm | 0.1 M KOH | Overpotential of 734 mV at 7.1 mA·cm$^{-2}$; Tafel slope of 120.9 mV·dec$^{-1}$ (*vs*. RHE) | [131], 2014 |
| Graphene[a] | In situ dissection | 5-7 layer | 1 M KOH | Overpotential of 1.8 V at 20.95 mA·cm$^{-2}$; Tafel slope of 43.1 mV·dec$^{-1}$ (*vs*. RHE) | [132], 2017 |

| | | | | | |
|---|---|---|---|---|---|
| Black Phosphorus[a] | Solution-phase exfoliation | 6 nm | 1 M KOH | Onset-potential 145mv; Tafel slope of 88 mV·dec$^{-1}$ (*vs.* RHE) | [133], 2017 |

[a] Representative 2D layered materials for comparison.

may hold a unique advantage for commercial overall water splitting applications.

### 4.3. Metal Organic Frameworks (MOFs)

MOFs are composed of coordination bonds between metal atom nodes and organic ligands with periodic structural units. Owing to their active transition metal centers and the uniform porous structure, MOFs are promising as electrocatalysts for OERs. Nevertheless, thin-film electrodes built on MOFs suffer from low conductivity, poor mass permeability, and blockage of active metal centers by organic ligands, which greatly limit their application in electrocatalysis. Thinning MOFs to a 2D morphology has been considered as an effective way to obtaining high performance MOFs-based OER electrocatalysts.[127, 128] The electron transfer and mass transport properties could be largely improved by the 2D MOF structure. In addition, the rich coordinatively unsaturated metal sites are favorable for adsorption and are the dominating active centers for OER.[128] Zhao *et al*. developed 2D NiCo MOF through a simple ultrasound method for OER electrocatalysis.[128] In $O_2$-saturated 1 M KOH solution at 5 mV scan rate, the 3.1 nm-thick NiCo MOF exhibited a much lower overpotential of 250 mV at 10 mA cm$^{-2}$ compared to bulky NiCo MOF nanosheets (317mV), Co MOF nanosheets (371 mV), Ni MOF nanosheets (321 mV), and commercial $RuO_2$ (279 mV). In addition to the large quantity of exposed coordinatively unsaturated surface metal atoms, the coupling effect between Co and Ni also made favorable contribution to the OER enhancement. XPS results indicated a part of electrons is transferred from $Ni^{2+}$ to $Co^{2+}$ through the oxygen of the ligands. Such coupling effect between Ni and Co could induce a change of $e_g$-orbital filling and benefit their OER performance.[134] The 2D NiCo MOF provided a promising alternative for heterogeneous electrocatalysts for OER under alkaline conditions.

## 5. Oxygen reduction reaction

The oxygen reduction reaction (ORR) is a critical reaction in fuel cells and metal-air batteries, where oxygen is reduced to $O^{2-}$ upon the receiving of electrons. The mechanism of ORR is complex and includes a multistep electron transfer process.[135, 136 137] As shown in **Figure 9a**, the reaction may go through two different pathways in an aqueous solution. One pathway is a four-electron (4e$^-$) process, where $O_2$ is directly reduced to $H_2O$ (in acid electrolytes) or $OH^-$ (in alkaline electrolytes). The other one includes two successive two-electron (2e$^-$) processes, which involves the production of peroxide intermediate (in acid electrolytes) or $HO_2^-$ intermediate (in alkaline electrolytes) from $O_2$.[30] In an ORR process, hydrogen can react with the oxygen either on the surface *via* the Langmuir–Hinschelwood (LH) mechanism, or in the electrolyte via the Eley–Rideal (ER) mechanism, depending on the reaction conditions.[138] The energy plots in **Figure 9b** present that both classes of reactions (LH and ER) possibly occurred at electrode potentials near 1.23 eV, and the corresponding reduction potential of the ORR was calculated by the Nernst equation. Individual ER reaction barriers are lower than the LH barriers at the ideal calculated potential of 0 V. With the applied electrode potential, the barrier heights of escaping bound O* and OH* intermediates can be changed, as presented in **Figure 9c**.

Recently, 2D non-layered materials showed promising application potential in ORR electrocatalysis. The 2D morphology-related advantages, such as a large number of surface active sites, enhanced charge/mass transport, and extensive contact area with electrolyte are playing an important role in boosting the ORR

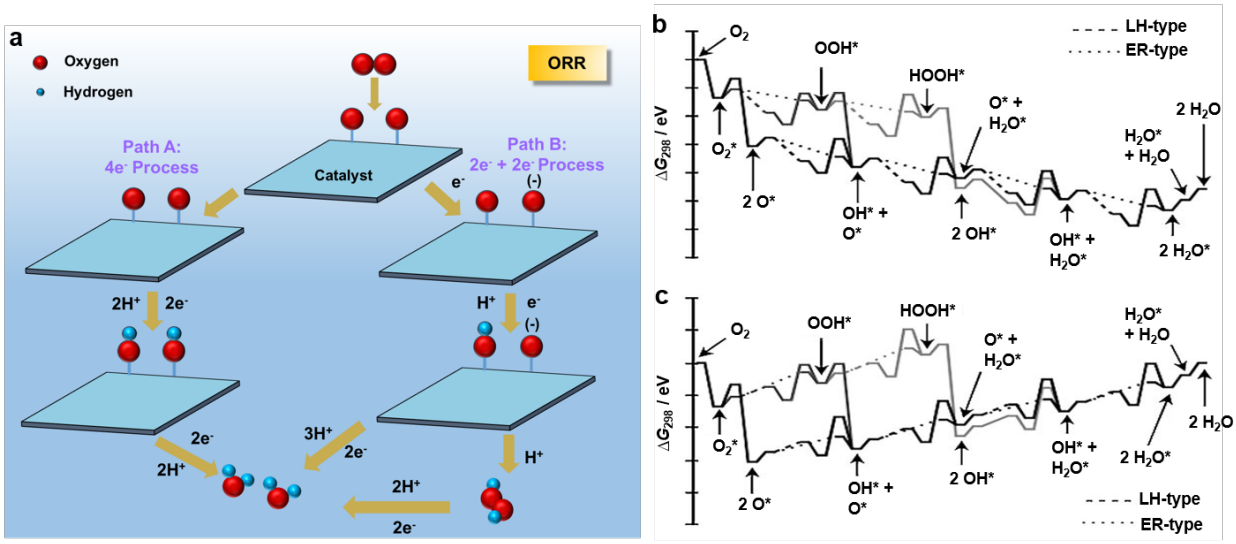


**Figure 9.** Mechanism of the ORR. (**a**) Schematic diagram of the ORR mechanism in aqueous media. [137]Reproduced with permission from © 1997 Elsevier Ltd. The energy plots of Langmuir–Hinschelwood (LH) and Eley–Rideal (ER) reaction mechanisms for the ORR (**b**) At the ideal calculated potential U = 0 V, (**c**) U = 1.14 eV (vs. RHE).[138]Reproduced with permission from © 2010 Wiley-VCH Verlag GmbH& Co. KgaA. Weinheim.

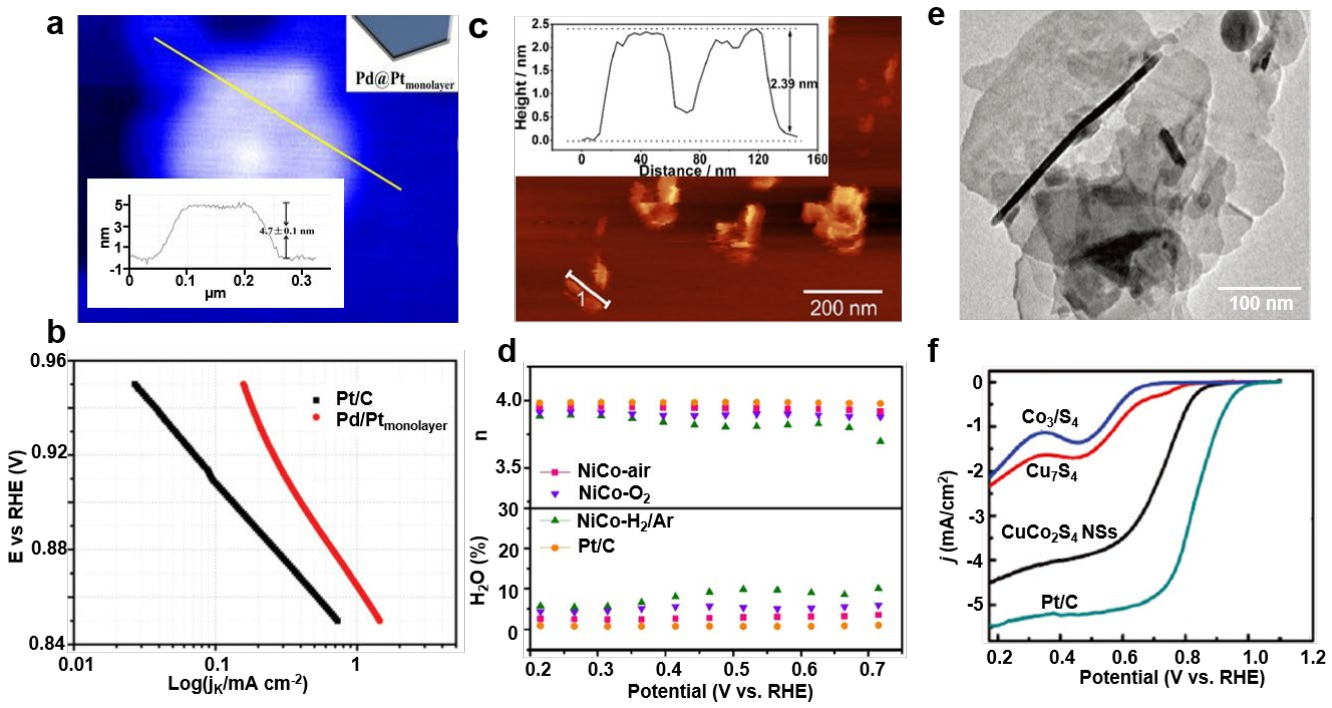


**Figure 10**. Different types of 2D non-layered materials for ORR. (**a**) AFM images of the core-shell structured 2D Pd@$Pt_{monolayer}$ and corresponding height details along the yellow line (**b**) The area-specific kinetic current densities ($j_K$) of 2D Pd@$Pt_{monolayer}$ and commercial Pt/C in the $O_2$-purged 0.1 M $HClO_4$ solution. [142]Reproduced with permission from © 2013 The Royal Society of Chemistry. (**c**) AFM image of the as prepared 2D $NiCo_2O_4$ calcined in air and corresponding height profile. (**d**) The electron transfer number and percentage of peroxide with respect to the total oxygen reduction products for 2D $NiCo_2O_4$ calcined in air, $O_2$, $H_2$/Ar, and the Pt/C electrode in the $O_2$-saturated 0.1 M KOH solution. [145]Reproduced with permission from © 2019 Elsevier B.V. (**e**) TEM image of 2D $CuCo_2S_4$. (**f**) ORR polarization plots of 2D $CuCo_2S_4$, $Cu_7S_4$ nanodisks, $Co_3S_4$ nanocrystals, and Pt/C catalysts in the $O_2$-saturated 0.1 M KOH solution at a rotation rate of 1600 rpm. [122]Reproduced with permission from © 2016 The Royal Society of Chemistry.

performance. Besides, although ORR requires the supply of electrons as HER, the surface needs to have strong affinity to oxygen species. Therefore, a number of 2D non-layered electrocatalysts have been developed for the ORR from metal oxides, metals, and MTCs, as they are good electronic conductors and possess low oxygen adsorption energies, which are favorable for the adsorption and reaction of oxygen on their surfaces. A chronological summary of 2D non-layered electrocatalysts for ORR is shown in **Table 3**.

### 5.1. Metals

In proton exchange membrane (PEM) fuel cells, the cathode usually requires a large amount of Pt to catalyze the sluggish ORR.[139-141] In order to reduce the cost of noble metal Pt, it is important to improve its utilization rate. The 2D morphology is a promising strategy to maximizing the specific surface area with desired catalytic activity and durability. Wang *et al*. synthesized 2D core–shell Pd@$Pt_{monolayer}$ on a Pd substrate that showed excellent electrocatalytic activity and stability for ORR in acidic electrolytes.[142] The use of Pd substrates was found beneficial to ORR activity, because it could reduce the surface oxygen affinity of Pt. Atomically smooth Pt skin was synthesized by defect - mediated membrane growth, following by the formation of Pd coating. The 2D Pd@$Pt_{monolayer}$ had a thickness of ~4.7 nm **(Figure 10a)**, and exhibited enhanced kinetic activities across the entire potential region compared to the commercial Pt/C (**Figure 10b**). The area-specific activity ($A_s$) of 2D Pd@$Pt_{monolayer}$ reached 0.438 A $cm^{-2}$ at 0.9 V, and its corresponding mass activity ($A_m$) was 0.717 A $mg^{-1}$. These $A_s$ and $A_m$ values were 3.4 and 6.6 times higher than those of the commercial Pt/C catalyst ($As$ = 0.128 A $cm^{-2}$, $Am$ = 0.109 A $mg^{-1}$), respectively, and reached the US DOE 2017 target for Pt based ORR catalysts ($A_m$ = 0.44 A $mg^{-1}$).[143] 2D materials from bimetallic Pt/Pd alloy were also reported for the ORR and similarly higher electrocatalytic activity was obtained compared to commercial Pt/C.[144]

### 5.2. Metal oxides

Due to their oxygen affinity and abundancy, metal oxides are a natural choice as ORR electrocatalysts. Among them, complex metal oxides such as $NiCo_2O_4$ and $ZnCo_2O_4$ often have higher activity of ORR compared to binary metal oxides.[145, 146] These oxides usually have a spinel structure, where the different octahedral metal ions in the spinel could facilitate the activation and cleavage of O-O bonds, and thus favorite ORR.[147] However, the activity of spinel oxides for ORR is still not sufficient for practical applications, such as Zn-air batteries. Improving their catalytic performance for ORR remains a critical challenge. Liu *et al*. synthesized 2D $NiCo_2O_4$ with a thickness of 2 nm for ORR (**Figure 10c**).[145] Owing to the ultrathin features and a high concentration of oxygen vacancies formed by oxygen-deficient calcination, the 2D $NiCo_2O_4$ exhibited improved electrocatalytic performance of ORR with an onset potential of 0.85 V. Zn-air batteries assembled from the 2D $NiCo_2O_4$ showed a comparable performance as commercial Pt/C. As shown in **Figure 10d**, the 2D $NiCo_2O_4$ materials calcined in air, $O_2$, and $H_2$/Ar were denoted as NiCo-air, NiCo-$O_2$, and NiCo-$H_2$/Ar, respectively. The electron transfer numbers of NiCo-$H_2$/Ar, NiCo-$O_2$, NiCo-air, and Pt/C were

3.80, 3.90, 3.94, and 3.99, respectively, which confirmed that the ORR processes mainly consisted of 4-electron reduction and the performance of NiCo-air was very close to commercial Pt/C. Meanwhile, the $HO_2$- yields of 2D NiCo-air were also close to commercial Pt/C. Zn-air batteries assembled from the 2D $NiCo_2O_4$ showed a smaller discharging/charging voltage gap and a higher stability compared to commercial Pt/C. The 2D structure significantly increased the number of active sites of these spinel oxides, demonstrating a good promise for replacing noble metal catalysts in ORR, such as in Zn-air battery applications.

**Table 3.** Summary of 2D non-layered materials reported for ORR electrocatalysts.

| Catalyst | Synthetic method (precursor) | Thickness | Electrolyte | Electrochemical performance | Refs., year |
|---|---|---|---|---|---|
| Core-shell Pd@$Pt_{monolayer}$ | Defect-mediated thin film growth method | 4.7 nm | 0.1 M $HClO_4$ | Half-wave potential of 0.874 V; Mass activity ($A_m$): 0.717 A $mg^{-1}$ at 0.9 V (*vs*. RHE) | [142], 2015 |
| PtPd alloy | Fast one-pot aqueous method (metal $PtCl_6^{2-}$ and $PdCl_4^{2-}$) | 6.0 nm | 0.1 M KOH | Half-wave potential of 0.879 V; Mass activity: 382.10 mA $mg^{-1}$ at 0.80 V (*vs*. RHE) | [144], 2019 |
| $Pt_{32}Pd_{48}Ni_{20}$ | A robust and general wetchemical route ($Pt(acac)_2$, $Pd(acac)_2$, $Ni(acac)_2$, $Mo(CO)_6$) | 1.4 nm | 0.1 M KOH | Mass activities: 0.54 A $mg^{-1}$ at 0.9 V (*vs*. RHE) | [148], 2019 |
| $NiCo_2O_4$ | Thermal treatment (Ni-Co hydroxide) | 2.4 nm | 0.1 M KOH | Onset potential of 0.85 V and half-wave potential of 0.74 V; Tafel slope of 68 mV·$dec^{-1}$ (vs. RHE) | [145], 2019 |
| $ZnCo_2O_4$ | Thermal treatment (Zn-Co-LDH) | Ultrathin | 0.1 M KOH | Average electron transfer number (n): 4.1 (*vs*. RHE) | [146], 2018 |
| $CuCo_2S_4$ | One -pot sulfurization ($Cu(acac)_2$, $Co(acac)_2$ dodecylamine, DDT) | 10-13 nm | 0.1 M KOH | Onset potential of 0.90 V; Half-wave potential of 0.74 V; Tafel slope: 74 mV $dec^{-1}$ (*vs*. RHE) | [122], 2016 |
| $FeNiS_2$ | A facile colloidal method ($Fe(acac)_3$, $Ni(aca)_2$, OTT, OAM, ODE) | 2-3 nm | 0.1 M KOH | Onset potential of 0.78 V; Current density: 3.2 mA $cm^{-2}$ at 0.45 V; Tafel slope: 107 mV $dec^{-1}$ (*vs*. RHE) | [149], 2016 |
| Pt embedded MOFs | Ultrasonication-assisted wet chemical method | 2-4 nm | 0.1 M KOH | Half-wave potentials of 75 mV (Co as the metal nodes); Half-wave potentials of 48 mV (Ni as the metal nodes); Electrons transferred: 4 (*vs*. RHE) | [150], 2018 |

### 5.3. TMCs

Because Cu- and Co- based nanocrystals were considered as good electrocatalysts for ORR, 2D TMCs of relevant compounds, such as $CuCo_2S_4$ and $FeNiS_2$, have also been studied for ORRs.[122, 149] Wang *et al*. adopt a "leveling metal activity and structure-directed one-pot sulfurization" strategy to prepare 2D $CuCo_2S_4$, which mainly exposed their (111), (022), and (004) facets.[122] The as-synthesized 2D $CuCo_2S_4$ had a circular sheet-like structure with a diameter of ~100-200 nm (**Figure 10e**). The LSV curve of 2D $CuCo_2S_4$ was compared to three other control catalysts for ORR on a rotating disk electrode with the rotation speed of 1600 rpm in the $O_2$- saturated 0.1 M KOH aqueous solution (**Figure 10f)**. The half-wave potential and onset potential of 2D $CuCo_2S_4$ were 0.74 and 0.90 V (*vs.* RHE), respectively. These values were higher than those of metal chalcogenides, such as $Cu_7S_4$ nanodisks, $Co_3S_4$ nanocrystals, and other reported ORR catalysts (*e.g.*, Pd-$H_3PW_{12}O_4$-$CMK_3$, defective $TiO_2$, delithiated $Li_{1-x}CoO_2$).[151-153] Although this ORR electrocatalytic activity was still slightly lower than that of commercial Pt/C, creating 2D morphology already demonstrated a strong potential of using earth-abundant materials to replace precious metal catalysts. The enhanced activity of 2D $CuCo_2S_4$ could be attributed to the component effect and efficient electronic coupling of the two metal cations with different oxidation states (+1 for Cu, +2.4 for Co), as well as the ultrathin 2D geometry. Similar enhancements were observed from other 2D non-layered TMCs such as $FeNiS_2$.[149] The 2D $FeNiS_2$ also exhibited superior ORR electrocatalytic activity over those of $Ni_9S_8$ nanorods and 2D FeS under the same conditions, as well as a long-term stability, suggesting they may be used as a practical noble metal-free electrocatalyst.

## 6. Electrocatalytic $CO_2$ reduction

Electroreduction of $CO_2$ with well-defined catalysts is a promising strategy to reduce the greenhouse effect and produce value-added products. The electroreduction is attractive due to the environmental compatibility coupling with carbon-free renewable energy sources such as solar, tidal, and wind.[154] Typically, an electrochemical reduction of $CO_2$ at electrode-electrolyte interfaces includes three major steps: (i) chemical adsorption of $CO_2$ on the surface of an electrocatalyst (cathode); (ii) electron transfer and/or proton migration to dissociate C=O bonds and/or to form C-H bonds; and (iii) the desorption of products from the catalyst surface. In $CO_2$ electroreduction, the crucial step is $CO_2$ activation, which involves one-electron transfer to form a radical anion ($CO_2^{\bullet-}$). However, $CO_2$ is chemically inert, which has a low electron affinity and a very large energy gap (13.7 eV) between its lowest unoccupied molecular orbital and highest occupied molecular orbital. The activation of $CO_2$ into the radical anion ($CO_2^{\bullet-}$) is thermodynamically unfavorable, which requires a high reduction potential of -1.9 V versus SHE.[155]

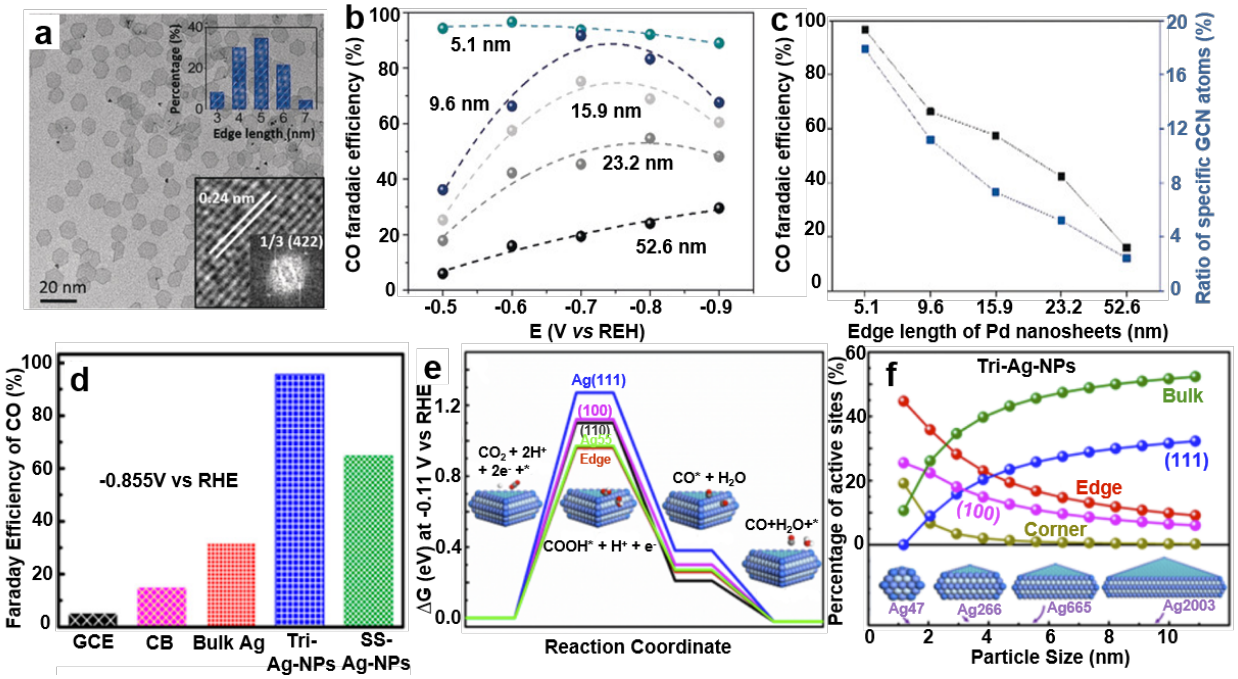


**Figure 11**. Different types of 2D metals for $CO_2$ reduction. (**a**) TEM images of 5.1 nm 2D Pd. Inset shows Pd edge length distribution and Fourier transform spectra. (**b**) Linear sweeping voltammetry of 2D Pd. (**c**) CO faradaic efficiency of 2D Pd with different edge lengths. [161]Reproduced with permission from © 2018 Wiley-VCH VerlagGmbH &Co. KGaA, Weinheim. (**d**) CO FEs at fixed potential of -0.855 V with 2D Ag catalyst. (**e**) Free energy diagrams for $CO_2$ reduction to CO on different facets of 2D Ag catalyst and $Ag_{55}$ cluster at -0.11 V. (**f**) active adsorption site density on Tri-Ag-NPs as a function of particle size. [162]Reproduced with permission from © 2017 American Chemical Society.

After the formation of $CO_2^{\bullet-}$ radicals, several proton-assisted multi-electron-transfer reactions can take place more efficiently, as these reactions are at lower energy costs compared to the first activation step. Based on the number of electrons and protons transferred, $CO_2$ can be reduced to different products, such as carbon monoxide (CO), formic acid (HCOOH), formaldehyde (HCHO), methanol ($CH_3OH$), methane ($CH_4$), ethylene ($C_2H_4$), ethanol ($C_2H_5OH$), and ethane ($C_2H_6$). A big challenge for electroreduction is the lack of the product selectivity due to the high activity of $CO_2^{\bullet-}$ radicals, small potential differences among various products, and the competitive side reaction, *e.g.* HER leading to the formation of $H_2$. Another concern is the stability of the electrocatalyst due to the deactivation by reaction intermediates, and byproducts. Due to the large number of low-coordinated surface atoms, 2D non-layered materials have recently attracted great attention for electrocatalytic $CO_2$ reduction. A summary of 2D non-layered electrocatalysts reported for $CO_2$ reduction is shown in **Table 4**. 2D Non-layered materials exhibit controllable electronic structures, high active site density, enhanced charge mobility, suitable binding affinity to carbon dioxide and/or reaction intermediates. These attractive properties lead to promising electrocatalyst with unique activity, selectivity, and stability.

### 6.1. Metals

Various metallic electrocatalysts such as Au, Pd, Ag, and Zn have been studied for $CO_2$ reduction.[156-160] The surface of these metals can bind CO weakly and exhibit relatively high $CO_2$ reduction efficiencies to CO rather than the competitive $H_2$ derived from HER. 2D metals with a substantial number of exposed active sites appeared to be beneficial for fast interfacial charge transfer and facile electrochemical catalysis. Recently, Zhu *et al*. observed that 2D Pd could effectively reduce the onset potential for CO formation by exposing abundant atoms with relatively low coordination number.[161] The as-synthesized 2D Pd were rather small, ranging from ~5 to 50 nm (**Figure 11a**). 2D materials with 5 atomic layer thickness and 5.1 nm edge length reached the CO faradaic efficiency of 94% at -0.5 V, which appeared to be the most efficient among all Pd based catalysts for $CO_2$ electroreduction (**Figure 11b**). Compared to similar-sized Pd nanoparticles, the 5.1 nm 2D Pd showed an over five times greater mass activity of 140 A $g^{-1}$ at -0.9 V. DFT calculations further demonstrated the enhanced catalytic activity was originated from more exposed atoms with an average coordination number of around 5 (**Figure 11c**).

Crystal facets also play a significant role in determining reaction activity and selectivity. Different surface facets show different Lewis acidity and polarizing power, thus influencing $CO_2$ adsorption and activation. A predominant shape-dependent electrocatalytic reduction of $CO_2$ to CO on 2D triangular silver nanoplates was demonstrated.[162] Triangular Ag nanoplates enclosed by the facets of (100) and (111) were synthesized through a wet-chemical approach. For $CO_2$ reduction reaction, this 2D Ag exhibited a higher Faraday efficiency (96.8%) for CO formation at a fixed potential of -0.855 V (vs RHE), as compared to similarly sized Ag nanoparticles and bulk Ag (**Figure 11d**). DFT calculations indicated that the high selectivity of CO at an ultralow overpotential stemmed from the combination of the predominant exposure of the (100) facets (**Figure 11e**) and the optimum edge-to-corner ratio (**Figure 11f**).

Although 2D metals with a very large amount of exposed surface atoms can be highly active $CO_2$ electroreduction catalysts, some of them tend to be very unstable at ambient conditions and can be

oxidized in an uncontrolled manner, which would lead to the loss of electronic conductivity and stability. 2D hybridization could avoid the oxidation of the highly reactive metals and improve the catalytic activity. Lei *et al*. reported highly reactive Sn quantum sheets confined in graphene showed enhanced electrocatalytic activity and stability.[163] The 2D Sn with lowered coordination numbers confined in graphene can efficiently stabilize the carbon dioxide radical anion.

In addition to increase the stability, 2D hybridization could also promote the selectivity towards $CO_2$ electroreduction. Dai *et al*. developed a simple strategy to prepare air stable 2D Cu/$Ni(OH)_2$. With a stable exposure of the Cu (111) facets, the hybrids exhibited high activity and selectivity for the reduction of $CO_2$ to CO, delivering a current density of 4.3 mA/cm$^2$ at a low overpotential of 0.39 V with a high faradaic efficiency (92%). Moreover, there was no obvious decay for catalytic performance over 22 h, indicating excellent stability for electroreduction of $CO_2$.[164] It has also been found that 2D hydridization could modify the binding strength of catalytic products on metal surfaces, and thus change the catalytic activies. Zhang *et al*. prepared 2D Pd partially capped by $SnO_2$ nanoparticles. Such a structure design not only enhanced the adsorption of $CO_2$ on $SnO_2$, but also weakened the binding strength of CO on Pd due to the as-built Pd–O–Sn interfaces, which was demonstrated to be critical to improve the electrocatalytic selectivity and stability of Pd catalysts. The hybrid 2D structure enabled multi-electron transfer for selective electroreduction of $CO_2$ into $CH_3OH$. [165]

**Table 4.** Summary of 2D non-layered materials reported for $CO_2$ reduction electrocatalysts.

| Catalysts | Synthetic method (precursor) | Thickness | Electrolytes | Current density | Overpotential | Products (FE) | Refs., year |
|---|---|---|---|---|---|---|---|
| Ag nanoplate | Chemical reduction ($AgNO_3$) | - | 0.1 M $KHCO_3$ | 1.2 mA cm$^{-2}$ @ −0.856 V (vs. RHE) | $\eta$: 0.45 V @ 1.2 mA cm$^{-2}$ | CO: 96.8%@ -0.855 V(vs. RHE) | [162], 2017 |
| Ag | Electrochemical oxidative–reductive approach | ~50 nm | 0.5 M $NaHCO_3$ | 10 mA cm$^{-2}$ @ −0.8 V (vs. RHE) | $\eta$: 0.29 V @ 5 mA cm$^{-2}$ | CO: 95% @ −0.7 V (vs. RHE) | [159], 2017 |
| Pd | CO-assisted method ($Pt(acac)_2$ DMF, PVP) | 5 atomic thickness | 0.1 M $KHCO_3$ solution | 14 mA cm$^{-2}$ @ -0.9V (vs. RHE) | Onset potential: −0.2 V (vs. RHE) | CO: 94% @ -0.5 V (vs. RHE) | [161], 2018 |
| Sn sheets confined in graphene | Spatially confined reduction strategy ($SnO_2$) | 1.4 nm | 0.1 M $NaHCO_3$ | 21.1 mA cm$^{-2}$@-1.8 V (vs. SCE) | Onset potential: −0.85 V (vs. SCE) | $HCOO^-$: 89% @ −1.8 V (vs. SCE) | [163], 2016 |
| $Co_3O_4$ | Fast-heating ($Co(CO_3)_{0.5}(OH)\cdot 0.11H_2O$) | 1.72 nm | 0.1 M $KHCO_3$ | 0.68 mA cm$^{-2}$ @ −0.88 V (vs. SCE) | Onset potential: −0.82 V (vs. SCE) | $HCOO^-$: 64.3% @ −0.88 V (vs. SCE) | [166], 2016 |
| Oxygen-deficient $Co_3O_4$ | Fast-heating process ($Co(CO_3)_{0.5}(OH)\cdot 0.11H_2O$) | 0.84 nm | 0.1 M $KHCO_3$ | 2.7 mA cm$^{-2}$ @ −0.87 V (vs. SCE) | Onset potential: −0.78 V (vs. SCE) | $HCOO^-$: 87.6% @ −0.87 V (vs. SCE) | [167], 2017 |
| Mesoporous $SnO_2$ | Calcination in air (2D $SnS_2$) | <10 nm | 0.5 M $NaHCO_3$ | 50 mA cm$^{-2}$ @ −1.6 V (vs. Ag/AgCl) | $\eta$: 0.88 V @ 45 mA cm$^{-2}$ | $HCOO^-$: 89% @ −1.6 V (vs. Ag/AgCl) | [168], 2017 |

A drastic enhancement in catalytic activity toward the electroreduction of $CO_2$ into formate was obtained from 2D Co.[169] Freestanding 2D Co with a thickness of only 4 atomic layers was synthesized by a ligand-confined growth strategy. The 2D morphology exhibited higher catalytic activity and selectivity towards formate production at a lower overpotential than bulk samples. It was argued that Co atoms confined in atomic layers were able to facilitate $CO_2$ activation by stabilizing the $CO_2^{\bullet-}$ intermediate more effectively than that could be achieved by their bulk counterpart. Partial oxidation of the atomic layers could further raise the activity and selectivity towards formate production. After partial oxidation, the 2D Co showed a stable current density of ~10 mA/cm$^2$ over 40 hours, with 90% formate selectivity at an overpotential of 0.24 V. Compared to bulk Co, these atomically thin sheets achieved a 260 times increase in current density. Partially oxidized 2D Co demonstrated a further enhanced $CO_2$ adsorption capacity, which promoted the intermediate reaction.

### 6.2. Metal oxides

2D Metal oxides have also been widely studied as $CO_2$ reduction electrocatalysts.[168, 170, 171] 2D Non-layered metal oxides with abundant low-coordinated surface metal cations could serve as the adsorption sites for $CO_2$ in the reduction processes and enhance $CO_2$ activation. Reduction in thickness could lead to significant increases in active sites and electrical conductivity, and thus improve the electrocatalytic activity. Gao *et al*. demonstrated that 1.72 nm 2D $Co_3O_4$ exhibited a higher electroreduction $CO_2$ activity than 3.51 nm 2D $Co_3O_4$ and bulk counterpart.[166] The thinner structure endowed 2D $Co_3O_4$ with a higher fraction of low-coordinated surface Co atoms, which could serve as the main adsorption sites for $CO_2$ in the reduction processes, hence ensuring a large amount of $CO_2$ adsorption, necessary for the subsequent reduction reactions. DFT calculations revealed that thinner 2D $Co_3O_4$ had a more dispersed charge density near Fermi level (**Figure 12a-b**), which was beneficial for increased electronic conductivity. As a result, 1.72 nm 2D $Co_3O_4$ had a current density of 0.68 mA cm$^{-2}$ at -0.88 V vs. SCE, over 1.5 and 20 times higher than that of 3.51 nm 2D $Co_3O_4$ and bulk counterpart, respectively (**Figure 12c**). The quick electron transport along the 2D ultrathin layer allowed for low corrosion rates and hence led to long-term durability in aqueous electrolyte. 1.72 nm 2D $Co_3O_4$ showed formate Faradaic efficiency of over 60 % in 20 h.

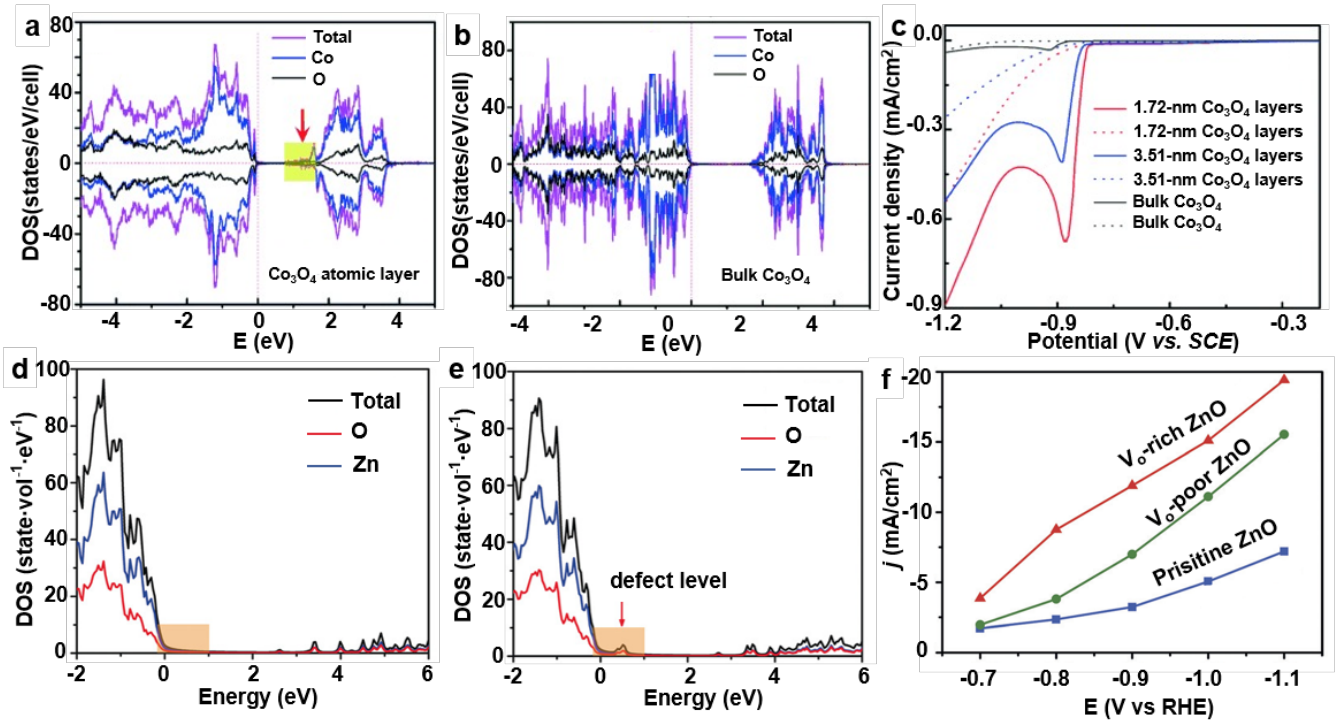


**Figure 12.** Different types of 2D metal oxides for $CO_2$ reduction. Calculated DOS for (**a**) 2D $Co_3O_4$ with a thickness of 1.72 nm and (**b**) bulk $Co_3O_4$ slab. The yellow shaded parts represent the increased DOS at the conduction band edges of $Co_3O_4$ atomic layer. (**c**) Linear sweep voltammetric curves for electroreduction of $CO_2$ into formate by 2D $Co_3O_4$ with different thicknesses in the $CO_2$ saturated (solid line) and $N_2$ saturated (dash line) 0.1 M $KHCO_3$ aqueous solution. [166]Reproduced with permission from @ 2016 Wiley-VCH Verlag GmbH &Co. KGaA, Weinheim. Calculated density of states of (**d**) 2D ZnO and (**e**) 2D ZnO with an oxygen vacancy. (**f**) Total current densities for CO production on the three 2D ZnO at selected potentials. [173]Reproduced with permission from @ 2018 Wiley-VCH Verlag GmbH &Co. KGaA, Weinheim.

2D non-layered materials possess abundant exposed surface atoms which can easily escape from the respective lattice to form vacancy-type defects. In oxides, O-vacancies can reduce the coordination number of the surface atoms and promote chemisorption of $CO_2$ molecules. $CO_2$ molecules are prone to adsorb at oxygen vacancies with one oxygen atom of $CO_2$ situated by bridging oxygen vacancy defects, thus decreasing the energy barrier for $CO_2$ activation.[172] Geng *et al*. developed 2D ZnO rich in O-vacancies as efficient catalysts towards $CO_2$ electrochemical reduction.[173] The O-vacancies were introduced by a facile $H_2$ plasma treatment. DFT calculations demonstrated that the introduction of O-vacancies increased the charge density of ZnO at the valence band maximum, resulting in enhanced activation of $CO_2$ (**Figure 12d-e**). In the $CO_2$ electrochemical reduction, O-deficient 2D ZnO exhibited a current density for CO production of -16.1 mA $cm^{-2}$ with a Faradaic efficiency of 83 % at -1.1 V versus RHE (**Figure 12f**). Mechanistic study revealed that O-vacancies improved binding strength of $CO_2$ and facilitated the activation of $CO_2$, leading to the superior kinetics for CO production. Similarly, Gao *et al*. demonstrated the role of O-vacancies confined in $Co_3O_4$ single-unit-cell layers for $CO_2$ electroreduction.[167] By comparing the 2D $Co_3O_4$ with high and low O-vacancy concentration, it was found that O-vacancies facilitated $CO_2$ adsorption as well as $HCOO^-$ desorption. Additionally, electro kinetic results demonstrated that proton transfer from $HCO_3^-$ was a rate-determining step. DFT calculations unveiled that O-vacancies could lower the rate-limiting activation barrier from 0.51 to 0.40 eV *via* stabilizing the $HCOO^{-}$* intermediates, as reflected by the lowered onset potential from 0.81 to 0.78 V and decreased Tafel slope from 48 to 37 $mVdec^{-1}$. O-vacancy-rich 2D $Co_3O_4$ exhibit a current density of 2.7 $mA/cm^2$ with ca. 85% formate selectivity during 40 h tests.

## 7. Conclusions and perspectives

In this review, we summarized recent progresses in emerging 2D non-layered materials for four representative types of electrocatalytic reactions. Various 2D non-layered catalysts including metals, metal oxides, metal chalcogenides, metal nitrides, and metal phosphides were reviewed systematically. We discussed the approaches and mechanisms of electronic structure modulation in 2D non-layer materials as an emerging platform for advanced electrocatalysis. Through thickness tuning, vacancy engineering, doping and hybridization, the electronic states of 2D materials could be effectively controlled and thus leading to significantly improved catalytic performance. Another unique and significant advantage for non-layered 2D materials is their extremely large ratio between surface atoms and bulk atoms, which can significantly reduce the mass requirement for precise elements in high-performance electrocatalyst designs. Compared to layered materials, 2D non-layered materials offer unique performance features towards electrocatalysis. Firstly, 2D non-layered materials possess numerous low-coordinated atoms at the surface, which are of great benefit for chemisorption of reactants, enabling highly chemically active surfaces and enhanced catalytic performance. Secondly, the large lattice structure distortion with massive surface dangling bonds modifies the electronic states at the surface, which significantly enhances the electrical conductivity and carrier mobility, enabling fast reaction kinetics. Third, the structural and electronic properties

of 2D non-layered materials can be tuned by structure and surface engineering, which can further manipulate the surface electronic states for enhanced performances in various catalytic applications.

***HER.*** HER is the most intensively studied electrocatalytic process using non-layered 2D materials, and many promising results have been obtained. However, there are still a few big challenges in achieving cost-effective electrocatalysis with catalytic activities matching those of noble metals (*i.e.*, Pt, Pd, and Rh). More research efforts are needed for controllable design and synthesis of non-layered materials from earth-abundant elements to realize higher ratio of exposed surface active sites, and well-engineered defects to reach desired $\Delta G_H$ and charge transfer kinetics. 2D metal alloys would be a promising new solution for developing low cost and high efficient non-noble metal HER catalysts due to the synergistic effect. Most 2D materials are restricted to strong acidic or alkaline electrolytes for achieving high HER activities. Electrocatalytic HER in neutral aqueous systems (*e.g.* seawater) remains a big challenge due to its low conductivity, ion poisoning, and high corrosivity. The intriguing structural and electronic properties of non-layered 2D materials, as well as various approaches used to control their morphology and electronic structures, could provide a new platform for exploring the HER in neutral electrolytes. Furthermore, lack of long-term stability and durability is a general problem for nanoscale catalysts. In this regard, selecting appropriate supporting materials to hybridize 2D materials could provide new opportunities to improve the longevity against air oxidation and electrocatalyst collapse.

***OER and ORR.*** Current research on 2D non-layered materials for OER and ORR is still far from mature. Due to the sluggish kinetics, the efficiency of most reported nanoscale catalysts remains insufficient to replace the costly commercial precious-metal-based electrocatalysts (*e.g.* Pt for ORR and $IrO_2$ for OER). The main research efforts should be devoted to either maximizing the atom efficiency of noble metal based electrocatalysts or developing high-performance electrocatalysts from earth-abundant materials. Achieving appropriate thermodynamic adsorption energies and kinetic reaction barriers in 2D catalysts design is essential to enhance the catalytic efficiency. Rational design and fine modulation of the electronic structure could be an effective pathway to further enhancement in catalytic performance. Possible methods include controlling the thickness, doping and alloying with other elements, and introducing structural heterogeneity. Thus far, the fundamentals of OER and ORR activities are still unclear in most 2D material systems rather than performance demonstrations. In situ characterization techniques combined with theoretical computation are highly desired to bring fundamental insights into the thickness and surface-related reaction kinetics, which are essential to build the structure–activity relationships in different material systems.

***$CO_2$ Reduction.*** Although advances have been made in electrocatalytic reduction of $CO_2$, most of the electrocatalysts are still facing low energetic efficiency, unsatisfactory selectivity and poor stability. Moreover, due to the complexity associated with multiple surface adsorption pattern and various reaction products, the fundamental mechanisms and kinetics of $CO_2$ adsorption, activation, multielectron transfer and desorption processes still need deeper understanding. Practically, costly noble metal catalysts were still primarily used to offer the highest efficiency. Currently, many research efforts have been focusing on the design and synthesis of cost-effective and stable electrocatalysts that can reduce $CO_2$ at high rates at minimum overpotential. Non-layered materials have been demonstrated to be an excellent choice for $CO_2$ reduction due to their unique structural and electronic properties. The large amount of low-coordinated metal atoms on the surface of metal or metal oxide 2D materials are favorable for stabilizing the $CO2^{\bullet-}$ intermediates, hence lowering the overall activation energy barrier and remarkably improving the catalytic activity. Structure modification of 2D non-layered materials would be an efficient pathway to achieve further enhancement in catalytic performance. Possible research directions include control of thickness, creating defects and heterogeneous interfaces, doping and alloying with other elements. Rational control of the thickness and defect levels of non-layered materials could effectively modulate the electron transfer kinetics and further tune the $CO_2$ reduction activity. It is also promising to explore multinary 2D materials to boost the performances. Combination of theory and experiment studies on the complex catalytic reaction pathways are desired to aid future catalyst design, particularly from earth-abundant materials that could take the advantage of 2D morphology to convert $CO_2$ to targeted products at sufficiently high reaction rate and efficiency.

In general, although the research of 2D non-layered materials for advanced electrocatalysis is just in its infancy, this new type of material has already showed great promises in catalyzing many electrochemical redox reactions. In the future, extensive efforts are needed to elucidate the details of the electrocatalysis mechanisms with 2D non-layered materials, as they currently remain poorly understood. With the help of atomic and electronic level mechanism understandings, together with advanced and scalable synthesis approaches, 2D non-layered materials will soon evolve into a new group of highly-efficient, cost-effective and sustainable electrocatalysts for a broad range of energy and environmental applications.

## Conflicts of interest

There are no conflicts to declare.

## Acknowledgements

This work was primarily supported by National Science Foundation DMR-1709025.

## Notes and references

1. Y. Dou, L. Zhang, X. Xu, Z. Sun, T. Liao and S. X. Dou, *Chem. Soc. Rev.*, 2017, **46**, 7338-7373.
2. D. L. Duong, S. J. Yun and Y. H. Lee, *ACS Nano*, 2017, **11**, 11803-11830.
3. C. Tan, X. Cao, X.-J. Wu, Q. He, J. Yang, X. Zhang, J. Chen, W. Zhao, S. Han, G.-H. Nam, M. Sindoro and H. Zhang, *Chem. Rev.*, 2017, **117**, 6225-6331.
4. R. Dong, T. Zhang and X. Feng, *Chem. Rev.*, 2018, **118**, 6189-6235.

5. J. Ji, J. Wen, Y. Shen, Y. Lv, Y. Chen, S. Liu, H. Ma and Y. Zhang, *Journal of the American Chemical Society*, 2017, **139**, 11698-11701.
6. Y. Lv, S. Chen, Y. Shen, J. Ji, Q. Zhou, S. Liu and Y. Zhang, *Journal of the American Chemical Society*, 2018, **140**, 2801-2804.
7. Z. Zhou, Y. Zhang, Y. Shen, S. Liu and Y. Zhang, *Chemical Society Reviews*, 2018, **47**, 2298-2321.
8. D. Han, D. Ni, Q. Zhou, J. Ji, Y. Lv, Y. Shen, S. Liu and Y. Zhang, *Advanced Functional Materials*, 2019, **29**, 1905576.
9. P. Giusto, D. Cruz, T. Heil, H. Arazoe, P. Lova, T. Aida, D. Comoretto, M. Patrini and M. Antonietti, *Advanced Materials*, 2020, **32**, 1908140.
10. S. N. Talapaneni, G. Singh, I. Y. Kim, K. AlBahily, A. a. H. Al-Muhtaseb, A. S. Karakoti, E. Tavakkoli and A. Vinu, *Advanced Materials*, 2020, **32**, 1904635.
11. Y. Xu, J. Xue, Q. Zhou, Y. Zheng, X. Chen, S. Liu, Y. Shen and Y. Zhang, *Angewandte Chemie International Edition*, 2020, **59**, 14498-14503.
12. H. Yang, Z. Wang, S. Liu, Y. Shen and Y. Zhang, *Chinese Chemical Letters*, 2020, DOI: https://doi.org/10.1016/j.cclet.2020.07.048.
13. Y. Zhang, Y. Song, Y. Shen, K. Chen, Q. Zhou, Y. Lv, H. Yang, E. Xu, S. Liu, L. Liu and Y. Zhang, *CCS Chemistry*, 2020, DOI: 10.31635/ccschem.20.202000361.
14. T. Zhao, Q. Zhou, Y. Lv, D. Han, K. Wu, L. Zhao, Y. Shen, S. Liu and Y. Zhang, *Angewandte Chemie International Edition*, 2020, **59**, 1139-1143.
15. Q. H. Wang, K. Kalantar-Zadeh, A. Kis, J. N. Coleman and M. S. Strano, *Nat. Nanotechnol.*, 2012, **7**, 699-712.
16. W. Tao, N. Kong, X. Ji, Y. Zhang, A. Sharma, J. Ouyang, B. Qi, J. Wang, N. Xie, C. Kang, H. Zhang, O. C. Farokhzad and J. S. Kim, *Chem. Soc. Rev.*, 2019, **48**, 2891-2912.
17. H. Liu, Y. Du, Y. Deng and P. D. Ye, *Chem. Soc. Rev.*, 2015, **44**, 2732-2743.
18. Q. Weng, X. Wang, X. Wang, Y. Bando and D. Golberg, *Chem. Soc. Rev.*, 2016, **45**, 3989-4012.
19. M. Zhao, Y. Huang, Y. Peng, Z. Huang, Q. Ma and H. Zhang, *Chem. Soc. Rev.*, 2018, **47**, 6267-6295.
20. D. Rhodes, S. H. Chae, R. Ribeiro-Palau and J. Hone, *Nat. Mater.*, 2019, **18**, 541-549.
21. Z. Zhang, P. Lin, Q. Liao, Z. Kang, H. Si and Y. Zhang, *Adv. Mater.*, 2019, **31**, 1806411.
22. X. Zhang, Q. Liao, S. Liu, Z. Kang, Z. Zhang, J. Du, F. Li, S. Zhang, J. Xiao, B. Liu, Y. Ou, X. Liu, L. Gu and Y. Zhang, *Nat. Commun.*, 2017, **8**, 15881.
23. L. Gao, Q. Liao, X. Zhang, X. Liu, L. Gu, B. Liu, J. Du, Y. Ou, J. Xiao, Z. Kang, Z. Zhang and Y. Zhang, *Adv. Mater.*, 2020, **32**, 1906646.
24. B. Liu, Q. Liao, X. Zhang, J. Du, Y. Ou, J. Xiao, Z. Kang, Z. Zhang and Y. Zhang, *ACS Nano*, 2019, **13**, 9057-9066.
25. K. S. Novoselov, D. Jiang, F. Schedin, T. J. Booth, V. V. Khotkevich, S. V. Morozov and A. K. Geim, *PNAS*, 2005, **102**, 10451-10453.
26. S. Ida, D. Shiga, M. Koinuma and Y. Matsumoto, *J. Am. Chem. Soc.*, 2008, **130**, 14038-14039.
27. M. Choucair, P. Thordarson and J. A. Stride, *Nat. Nanotechnol.*, 2008, **4**, 30.
28. D. Wei, Y. Liu, Y. Wang, H. Zhang, L. Huang and G. Yu, *Nano Lett.*, 2009, **9**, 1752-1758.
29. W. Strupinski, K. Grodecki, A. Wysmolek, R. Stepniewski, T. Szkopek, P. E. Gaskell, A. Grüneis, D. Haberer, R. Bozek, J. Krupka and J. M. Baranowski, *Nano Lett.*, 2011, **11**, 1786-1791.
30. H. Jin, C. Guo, X. Liu, J. Liu, A. Vasileff, Y. Jiao, Y. Zheng and S.-Z. Qiao, *Chem. Rev.*, 2018, **118**, 6337-6408.
31. J. Di, C. Yan, A. D. Handoko, Z. W. Seh, H. Li and Z. Liu, *Mater. Today*, 2018, **21**, 749-770.
32. J. Di, J. Xiong, H. Li and Z. Liu, *Adv. Mater.*, 2018, **30**, 1704548.
33. M. P. Browne, Z. Sofer and M. Pumera, *Energy Environ. Sci.*, 2019, **12**, 41-58.
34. Y. Zhu, L. Peng, Z. Fang, C. Yan, X. Zhang and G. Yu, *Adv. Mater.*, 2018, **30**, 1706347.
35. F. Wang, J.-H. Seo, G. Luo, M. B. Starr, Z. Li, D. Geng, X. Yin, S. Wang, D. G. Fraser, D. Morgan, Z. Ma and X. Wang, *Nat. Commun.*, 2016, **7**, 10444.
36. C. Schliehe, B. H. Juarez, M. Pelletier, S. Jander, D. Greshnykh, M. Nagel, A. Meyer, S. Foerster, A. Kornowski, C. Klinke and H. Weller, *Science*, 2010, **329**, 550-553.
37. Y. Sun, Z. Sun, S. Gao, H. Cheng, Q. Liu, J. Piao, T. Yao, C. Wu, S. Hu, S. Wei and Y. Xie, *Nat. Commun.*, 2012, **3**, 1057.
38. L. Liang, H. Cheng, F. Lei, J. Han, S. Gao, C. Wang, Y. Sun, S. Qamar, S. Wei and Y. Xie, *Angew. Chem. Int. Ed.*, 2015, **54**, 12004-12008.
39. X. Huang, S. Li, Y. Huang, S. Wu, X. Zhou, S. Li, C. L. Gan, F. Boey, C. A. Mirkin and H. Zhang, *Nat. Commun.*, 2011, **2**, 292.
40. X. Xiao, H. Wang, P. Urbankowski and Y. Gogotsi, *Chem. Soc. Rev.*, 2018, **47**, 8744-8765.
41. F. Wang, Z. Wang, T. A. Shifa, Y. Wen, F. Wang, X. Zhan, Q. Wang, K. Xu, Y. Huang, L. Yin, C. Jiang and J. He, *Adv. Funct. Mater.*, 2017, **27**, 1603254.
42. C. Tan and H. Zhang, *Nat. Commun.*, 2015, **6**, 7873.
43. X. Zhang, Z. Zhang, J. Liang, Y. Zhou, Y. Tong, Y. Wang and X. Wang, *J. Mater. Chem. A*, 2017, **5**, 9702-9708.
44. X. Yin, Y. Shi, Y. Wei, Y. Joo, P. Gopalan, I. Szlufarska and X. Wang, *Langmuir*, 2017, **33**, 7708-7714.
45. Y. Sun, F. Lei, S. Gao, B. Pan, J. Zhou and Y. Xie, *Angew. Chem. Int. Ed.*, 2013, **52**, 10569-10572.
46. G. Yan, Y. Wang, Z. Zhang, Y. Dong, J. Wang, C. Carlos, P. Zhang, Z. Cao, Y. Mao and X. Wang, *Nano-Micro Lett.*, 2020, **12**, 49.
47. H. L. Qin, D. Wang, Z. L. Huang, D. M. Wu, Z. C. Zeng, B. Ren, K. Xu and J. Jin, *J. Am. Chem. Soc.*, 2013, **135**, 12544-12547.
48. M. Zhou, M. Lin, L. Chen, Y. Wang, X. Guo, L. Peng, X. Guo and W. Ding, *Chem. Commun.*, 2015, **51**, 5116-5119.
49. Y. Han, Y. Yan, Z. Wu, Y. Jiang, X. Li, Q. Xu, X. Yang, H. Zhang and D. Yang, *CrystEngComm*, 2018, **20**, 4230-4236.
50. H. Zhao, Y. Zhu, F. Li, R. Hao, S. Wang and L. Guo, *Angew. Chem. Int. Ed.*, 2017, **56**, 8766-8770.
51. X. Yin, Y. Wang, T.-h. Chang, P. Zhang, J. Li, P. Xue, Y. Long, J. L. Shohet, P. M. Voyles, Z. Ma and X. Wang, *Adv. Mater.*, 2020, **n/a**, 2000801.
52. X. Yin, Q. Chen, P. Tian, P. Zhang, Z. Zhang, P. M. Voyles and X. Wang, *Chem. Mater.*, 2018, **30**, 3308-3314.
53. F. Wang, Y. Yu, X. Yin, P. Tian and X. Wang, *J. Mater. Chem. A*, 2017, **5**, 9060-9066.
54. Y. Wang, Y. Shi, Z. Zhang, C. Carlos, C. Zhang, K. Bhawnani, J. Li, J. Wang, P. M. Voyles, I. Szlufarska and X. Wang, *Chem. Mater.*, 2019, **31**, 9040-9048.
55. M. Lyu, Y. Liu, Y. Zhi, C. Xiao, B. Gu, X. Hua, S. Fan, Y. Lin, W. Bai, W. Tong, Y. Zou, B. Pan, B. Ye and Y. Xie, *J. Am. Chem. Soc.*, 2015, **137**, 15043-15048.

56. Y. Liu, C. Xiao, P. Huang, M. Cheng and Y. Xie, *Chem*, 2018, **4**, 1263-1283.
57. F. Lei, Y. Sun, K. Liu, S. Gao, L. Liang, B. Pan and Y. Xie, *J. Am. Chem. Soc.*, 2014, **136**, 6826-6829.
58. Y. Liu, H. Cheng, M. Lyu, S. Fan, Q. Liu, W. Zhang, Y. Zhi, C. Wang, C. Xiao, S. Wei, B. Ye and Y. Xie, *J. Am. Chem. Soc.*, 2014, **136**, 15670-15675.
59. Y. Sun, Q. Liu, S. Gao, H. Cheng, F. Lei, Z. Sun, Y. Jiang, H. Su, S. Wei and Y. Xie, *Nat. Commun.*, 2013, **4**, 2899.
60. Y. Sun, S. Gao, F. Lei, J. Liu, L. Liang and Y. Xie, *Chem. Sci.*, 2014, **5**, 3976-3982.
61. Y. Liu, L. Liang, C. Xiao, X. Hua, Z. Li, B. Pan and Y. Xie, *Adv. Energy Mater.*, 2016, **6**, 1600437.
62. X. Yin, Y. Wang, R. Jacobs, Y. Shi, I. Szlufarska, D. Morgan and X. Wang, *Nano Lett.*, 2019, **19**, 7085-7092.
63. L. Xu, Q. Jiang, Z. Xiao, X. Li, J. Huo, S. Wang and L. Dai, *Angewandte Chemie International Edition*, 2016, **55**, 5277-5281.
64. H. Zhang, Q. Liu, J. Xu, L. Wei, Q. Liu and X. Kong, *Inorg. Chem.*, 2019, **58**, 8267-8270.
65. F. Lei, L. Zhang, Y. Sun, L. Liang, K. Liu, J. Xu, Q. Zhang, B. Pan, Y. Luo and Y. Xie, *Angew. Chem. Int. Ed.*, 2015, **54**, 9266-9270.
66. Y. Liu, X. Hua, C. Xiao, T. Zhou, P. Huang, Z. Guo, B. Pan and Y. Xie, *J. Am. Chem. Soc.*, 2016, **138**, 5087-5092.
67. H. Duan, N. Yan, R. Yu, C.-R. Chang, G. Zhou, H.-S. Hu, H. Rong, Z. Niu, J. Mao, H. Asakura, T. Tanaka, P. J. Dyson, J. Li and Y. Li, *Nat. Commun.*, 2014, **5**, 3093.
68. X. Huang, S. Tang, X. Mu, Y. Dai, G. Chen, Z. Zhou, F. Ruan, Z. Yang and N. Zheng, *Nat. Nanotechnol.*, 2011, **6**, 28-32.
69. M. Luo, Y. Yang, Y. Sun, Y. Qin, C. Li, Y. Li, M. Li, S. Zhang, D. Su and S. Guo, *Mater. Today*, 2019, **23**, 45-56.
70. X. Kong, K. Xu, C. Zhang, J. Dai, S. Norooz Oliaee, L. Li, X. Zeng, C. Wu and Z. Peng, *ACS Catal.*, 2016, **6**, 1487-1492.
71. Y. Kuang, G. Feng, P. Li, Y. Bi, Y. Li and X. Sun, *Angew. Chem. Int. Ed.*, 2016, **55**, 693-697.
72. L. Dai, Y. Zhao, Q. Qin, X. Zhao, C. Xu and N. Zheng, *ChemNanoMat*, 2016, **2**, 776-780.
73. Q. Zhang, P. Li, D. Zhou, Z. Chang, Y. Kuang and X. Sun, *Small*, 2017, **13**, 1701648.
74. A. Mahmood, H. Lin, N. Xie and X. Wang, *Chem. Mater.*, 2017, **29**, 6329-6335.
75. X. Zhao, L. Dai, Q. Qin, F. Pei, C. Hu and N. Zheng, *Small*, 2017, **13**, 1602970.
76. H. Liang, L. Li, F. Meng, L. Dang, J. Zhuo, A. Forticaux, Z. Wang and S. Jin, *Chem. Mater.*, 2015, **27**, 5702-5711.
77. X. Long, G. Li, Z. Wang, H. Zhu, T. Zhang, S. Xiao, W. Guo and S. Yang, *J. Am. Chem. Soc.*, 2015, **137**, 11900-11903.
78. L. Ma, Y. Hu, R. Chen, G. Zhu, T. Chen, H. Lv, Y. Wang, J. Liang, H. Liu, C. Yan, H. Zhu, Z. Tie, Z. Jin and J. Liu, *Nano Energy*, 2016, **24**, 139-147.
79. F. Wang, Y. Li, T. A. Shifa, K. Liu, F. Wang, Z. Wang, P. Xu, Q. Wang and J. He, *Angew. Chem. Int. Ed.*, 2016, **55**, 6919-6924.
80. C. Zhang, Y. Shi, Y. Yu, Y. Du and B. Zhang, *ACS Catal.*, 2018, **8**, 8077-8083.
81. H. Wu, X. Lu, G. Zheng and G. W. Ho, *Adv. Energy Mater.*, 2018, **8**, 1702704.
82. D. Gao, J. Zhang, T. Wang, W. Xiao, K. Tao, D. Xue and J. Ding, *J. Mater. Chem. A*, 2016, **4**, 17363-17369.
83. H. Jin, X. Liu, A. Vasileff, Y. Jiao, Y. Zhao, Y. Zheng and S.-Z. Qiao, *ACS Nano*, 2018, **12**, 12761-12769.
84. Z. Pu, Q. Liu, P. Jiang, A. M. Asiri, A. Y. Obaid and X. Sun, *Chem. Mater.*, 2014, **26**, 4326-4329.
85. X. Wang, Y. V. Kolen'ko, X.-Q. Bao, K. Kovnir and L. Liu, *Angewandte Chemie International Edition*, 2015, **54**, 8188-8192.
86. X.-D. Wang, Y.-F. Xu, H.-S. Rao, W.-J. Xu, H.-Y. Chen, W.-X. Zhang, D.-B. Kuang and C.-Y. Su, *Energy & Environmental Science*, 2016, **9**, 1468-1475.
87. Z. Pu, S. Wei, Z. Chen and S. Mu, *Appl. Catal. B*, 2016, **196**, 193-198.
88. L. Zhou, M. Shao, J. Li, S. Jiang, M. Wei and X. Duan, *Nano Energy*, 2017, **41**, 583-590.
89. C. Zhang, Y. Huang, Y. Yu, J. Zhang, S. Zhuo and B. Zhang, *Chem. Sci.*, 2017, **8**, 2769-2775.
90. H. Li, X. Zhao, H. Liu, S. Chen, X. Yang, C. Lv, H. Zhang, X. She and D. Yang, *Small*, 2018, **14**, 1802824.
91. T. Li, H. Jin, Z. Liang, L. Huang, Y. Lu, H. Yu, Z. Hu, J. Wu, B. Y. Xia, G. Feng and J. Zhou, *Nanoscale*, 2018, **10**, 6844-6849.
92. X. Zhang, J. Ji, Q. Yang, L. Zhao, Q. Yuan, Y. Hao, P. Jin and L. Feng, *ChemCatChem*, 2019, **0**.
93. X. Liu, B. Wei, R. Su, C. Zhao, D. Dai, X. Ma and L. Xu, *Energy Technol.*, 2019, **0**, 1900021.
94. A. Kumatani, C. Miura, H. Kuramochi, T. Ohto, M. Wakisaka, Y. Nagata, H. Ida, Y. Takahashi, K. Hu, S. Jeong, J.-i. Fujita, T. Matsue and Y. Ito, *Advanced Science*, 2019, **6**, 1900119.
95. Z. Pei, J. Gu, Y. Wang, Z. Tang, Z. Liu, Y. Huang, Y. Huang, J. Zhao, Z. Chen and C. Zhi, *ACS Nano*, 2017, **11**, 6004-6014.
96. Y. Yin, J. Han, Y. Zhang, X. Zhang, P. Xu, Q. Yuan, L. Samad, X. Wang, Y. Wang, Z. Zhang, P. Zhang, X. Cao, B. Song and S. Jin, *Journal of the American Chemical Society*, 2016, **138**, 7965-7972.
97. Y. Sun, X. Zhang, B. Mao and M. Cao, *Chemical Communications*, 2016, **52**, 14266-14269.
98. W. Chen, J. Gu, Y. Du, F. Song, F. Bu, J. Li, Y. Yuan, R. Luo, Q. Liu and D. Zhang, *Advanced Functional Materials*, 2020, **30**, 2000551.
99. M. M. Jaksic and J. M. Jaksic, *Electrochim. Acta*, 1994, **39**, 1695-1714.
100. M. Metikoš-Huković and A. Jukić, *Electrochim. Acta*, 2000, **45**, 4159-4170.
101. D. Zhang, H. Zhao, B. Huang, B. Li, H. Li, Y. Han, Z. Wang, X. Wu, Y. Pan, Y. Sun, X. Sun, J. Lai and L. Wang, *ACS Cent. Sci.*, 2019, **5**, 1991-1997.
102. X. Wang, R. Su, H. Aslan, J. Kibsgaard, S. Wendt, L. Meng, M. Dong, Y. Huang and F. Besenbacher, *Nano Energy*, 2015, **12**, 9-18.
103. T. F. Jaramillo, K. P. Jørgensen, J. Bonde, J. H. Nielsen, S. Horch and I. Chorkendorff, *Science*, 2007, **317**, 100-102.
104. B. Song, K. Li, Y. Yin, T. Wu, L. Dang, M. Cabán-Acevedo, J. Han, T. Gao, X. Wang, Z. Zhang, J. R. Schmidt, P. Xu and S. Jin, *ACS Catal.*, 2017, **7**, 8549-8557.
105. J. Xie and Y. Xie, *Chemistry – A European Journal*, 2016, **22**, 3588-3598.
106. H.-P. Guo, B.-Y. Ruan, W.-B. Luo, J. Deng, J.-Z. Wang, H.-K. Liu and S.-X. Dou, *ACS Catal.*, 2018, **8**, 9686-9696.
107. P. Jiang, Q. Liu and X. Sun, *Nanoscale*, 2014, **6**, 13440-13445.
108. Y. Shi and B. Zhang, *Chem. Soc. Rev.*, 2016, **45**, 1529-1541.

109. Y. Zhao, X. Jia, G. Chen, L. Shang, G. I. N. Waterhouse, L.-Z. Wu, C.-H. Tung, D. O'Hare and T. Zhang, *J. Am. Chem. Soc.*, 2016, **138**, 6517-6524.
110. S. M. Pawar, B. S. Pawar, B. Hou, J. Kim, A. T. Aqueel Ahmed, H. S. Chavan, Y. Jo, S. Cho, A. I. Inamdar, J. L. Gunjakar, H. Kim, S. Cha and H. Im, *J. Mater. Chem. A*, 2017, **5**, 12747-12751.
111. Y. Dou, T. Liao, Z. Ma, D. Tian, Q. Liu, F. Xiao, Z. Sun, J. Ho Kim and S. Xue Dou, *Nano Energy*, 2016, **30**, 267-275.
112. Y. Huang, X. Zhao, F. Tang, X. Zheng, W. Cheng, W. Che, F. Hu, Y. Jiang, Q. Liu and S. Wei, *J. Mater. Chem. A*, 2018, **6**, 3202-3210.
113. L. Xu, Z. Wang, J. Wang, Z. Xiao, X. Huang, Z. Liu and S. Wang, *Nanotechnology*, 2017, **28**, 165402.
114. P. Tian, Y. Yu, X. Yin and X. Wang, *Nanoscale*, 2018, **10**, 5054-5059.
115. J. Bao, X. Zhang, B. Fan, J. Zhang, M. Zhou, W. Yang, X. Hu, H. Wang, B. Pan and Y. Xie, *Angew. Chem. Int. Ed.*, 2015, **54**, 7399-7404.
116. Y. Li, F.-M. Li, X.-Y. Meng, S.-N. Li, J.-H. Zeng and Y. Chen, *ACS Catalysis*, 2018, **8**, 1913-1920.
117. S. Jin, *ACS Energy Lett.*, 2017, **2**, 1937-1938.
118. L. Peng, S. S. A. Shah and Z. Wei, *Chinese J. Catal.*, 2018, **39**, 1575-1593.
119. H. Liu, C.-Y. Xu, Y. Du, F.-X. Ma, Y. Li, J. Yu and L. Zhen, *Sci. Rep.*, 2019, **9**, 1951.
120. R. Souleymen, Z. Wang, C. Qiao, M. Naveed and C. Cao, *J. Mater. Chem. A*, 2018, **6**, 7592-7607.
121. Y. Liu, C. Xiao, M. Lyu, Y. Lin, W. Cai, P. Huang, W. Tong, Y. Zou and Y. Xie, *Angew. Chem. Int. Ed.*, 2015, **54**, 11231-11235.
122. S. Zhao, Y. Wang, Q. Zhang, Y. Li, L. Gu, Z. Dai, S. Liu, Y.-Q. Lan, M. Han and J. Bao, *Inorg. Chem. Front.*, 2016, **3**, 1501-1509.
123. Y. Li, J. Yin, L. An, M. Lu, K. Sun, Y.-Q. Zhao, D. Gao, F. Cheng and P. Xi, *Small*, 2018, **14**, 1801070.
124. R. Wei, M. Fang, G. Dong, C. Lan, L. Shu, H. Zhang, X. Bu and J. C. Ho, *ACS Appl. Mater. Interfaces*, 2018, **10**, 7079-7086.
125. L. Zhuang, L. Ge, Y. Yang, M. Li, Y. Jia, X. Yao and Z. Zhu, *Adv. Mater.*, 2017, **29**, 1606793.
126. L. Zhuang, Y. Jia, T. He, A. Du, X. Yan, L. Ge, Z. Zhu and X. Yao, *Nano Res.*, 2018, **11**, 3509-3518.
127. Y. Xu, B. Li, S. Zheng, P. Wu, J. Zhan, H. Xue, Q. Xu and H. Pang, *J. Mater. Chem. A*, 2018, **6**, 22070-22076.
128. S. Zhao, Y. Wang, J. Dong, C.-T. He, H. Yin, P. An, K. Zhao, X. Zhang, C. Gao, L. Zhang, J. Lv, J. Wang, J. Zhang, A. M. Khattak, N. A. Khan, Z. Wei, J. Zhang, S. Liu, H. Zhao and Z. Tang, *Nat. Energy*, 2016, **1**, 16184.
129. M. Qin, S. Li, Y. Zhao, C.-Y. Lao, Z. Zhang, L. Liu, F. Fang, H. Wu, B. Jia, Z. Liu, W. Wang, Y. Liu and X. Qu, *Advanced Energy Materials*, 2019, **9**, 1803060.
130. J. Wu, M. Liu, K. Chatterjee, K. P. Hackenberg, J. Shen, X. Zou, Y. Yan, J. Gu, Y. Yang, J. Lou and P. M. Ajayan, *Advanced Materials Interfaces*, 2016, **3**, 1500669.
131. J. Tian, Q. Liu, A. M. Asiri, K. A. Alamry and X. Sun, *ChemSusChem*, 2014, **7**, 2125-2130.
132. Z. Liu, Z. Zhao, Y. Wang, S. Dou, D. Yan, D. Liu, Z. Xia and S. Wang, *Advanced Materials*, 2017, **29**, 1606207.
133. X. Ren, J. Zhou, X. Qi, Y. Liu, Z. Huang, Z. Li, Y. Ge, S. C. Dhanabalan, J. S. Ponraj, S. Wang, J. Zhong and H. Zhang, *Advanced Energy Materials*, 2017, **7**, 1700396.
134. J. Suntivich, K. J. May, H. A. Gasteiger, J. B. Goodenough and Y. Shao-Horn, *Science*, 2011, **334**, 1383.
135. H. Tao, Y. Gao, N. Talreja, F. Guo, J. Texter, C. Yan and Z. Sun, *J. Mater. Chem. A*, 2017, **5**, 7257-7284.
136. D. Mukherjee and S. Sampath, in *2D Inorganic Materials beyond Graphene*, World Scientific, 2016, pp. 103-136.
137. G. J. K. Acres, J. C. Frost, G. A. Hards, R. J. Potter, T. R. Ralph, D. Thompsett, G. T. Burstein and G. J. Hutchings, *Catalysis Today*, 1997, **38**, 393-400.
138. J. A. Keith, G. Jerkiewicz and T. Jacob, *ChemPhysChem*, 2010, **11**, 2779-2794.
139. D. C. Higgins, R. Wang, M. A. Hoque, P. Zamani, S. Abureden and Z. Chen, *Nano Energy*, 2014, **10**, 135-143.
140. A. W. Marc Koper, *Fuel Cell Catalysis: A Surface Science Approach*, 2009, John Wiley & Sons Inc., New York.
141. J. Zhang, *PEM Fuel Cell Electrocatalysts and Catalyst Layers: Fundamentals and Applications*, 2008, Springer, New York.
142. W. Wang, Y. Zhao and Y. Ding, *Nanoscale*, 2015, **7**, 11934-11939.
143. M. K. Debe, *Nature*, 2012, **486**, 43-51.
144. H.-Y. Chen, M.-X. Jin, L. Zhang, A.-J. Wang, J. Yuan, Q.-L. Zhang and J.-J. Feng, *J. Colloid Interf. Sci.*, 2019, **543**, 1-8.
145. W. Liu, J. Bao, L. Xu, M. Guan, Z. Wang, J. Qiu, Y. Huang, J. Xia, Y. Lei and H. Li, *Appl. Surf. Sci.*, 2019, **478**, 552-559.
146. J. Bao, Z. Wang, W. Liu, L. Xu, F. Lei, J. Xie, Y. Zhao, Y. Huang, M. Guan and H. Li, *J. Alloys Compd.*, 2018, **764**, 565-573.
147. Y. Wang, J. Li and Z. Wei, *J. Mater. Chem. A*, 2018, **6**, 8194-8209.
148. J. Lai, F. Lin, Y. Tang, P. Zhou, Y. Chao, Y. Zhang and S. Guo, *Adv. Energy Mater.*, 2019, **9**, 1800684.
149. J. Jiang, S. Lu, H. Gao, X. Zhang and H.-Q. Yu, *Nano Energy*, 2016, **27**, 526-534.
150. Z. Xia, J. Fang, X. Zhang, L. Fan, A. J. Barlow, T. Lin, S. Wang, G. G. Wallace, G. Sun and X. Wang, *Appl. Catal. B*, 2019, **245**, 389-398.
151. T. Maiyalagan, K. A. Jarvis, S. Therese, P. J. Ferreira and A. Manthiram, *Nat. Commun.*, 2014, **5**, 3949.
152. D.-N. Pei, L. Gong, A.-Y. Zhang, X. Zhang, J.-J. Chen, Y. Mu and H.-Q. Yu, *Nat. Commun.*, 2015, **6**, 8696.
153. H. Liu, Y. Zheng, G. Wang and S. Z. Qiao, *Adv. Energy Mater.*, 2015, **5**, 1401186.
154. A. Zhang, R. He, H. Li, Y. Chen, T. Kong, K. Li, H. Ju, J. Zhu, W. Zhu and J. Zeng, *Angew. Chem. Int. Ed.*, 2018, **57**, 10954-10958.
155. D. D. Zhu, J. L. Liu and S. Z. Qiao, *Adv. Mater.*, 2016, **28**, 3423-3452.
156. B. A. Rosen, A. Salehi-Khojin, M. R. Thorson, W. Zhu, D. T. Whipple, P. J. A. Kenis and R. I. Masel, *Science*, 2011, **334**, 643-644.
157. W. Zhu, Y.-J. Zhang, H. Zhang, H. Lv, Q. Li, R. Michalsky, A. A. Peterson and S. Sun, *J. Am. Chem. Soc.*, 2014, **136**, 16132-16135.
158. D. Gao, H. Zhou, J. Wang, S. Miao, F. Yang, G. Wang, J. Wang and X. Bao, *J. Am. Chem. Soc.*, 2015, **137**, 4288-4291.
159. C.-Y. Lee, Y. Zhao, C. Wang, D. R. G. Mitchell and G. G. Wallace, *Sustain. Energy Fuels*, 2017, **1**, 1023-1027.
160. F. Quan, D. Zhong, H. Song, F. Jia and L. Zhang, *J. Mater. Chem. A*, 2015, **3**, 16409-16413.
161. W. Zhu, L. Zhang, P. Yang, C. Hu, Z. Luo, X. Chang, Z.-J. Zhao and J. Gong, *Angew. Chem. Int. Ed.*, 2018, **130**, 11718-11722.

162. S. Liu, H. Tao, L. Zeng, Q. Liu, Z. Xu, Q. Liu and J.-L. Luo, *J. Am. Chem. Soc.*, 2017, **139**, 2160-2163.
163. F. Lei, W. Liu, Y. Sun, J. Xu, K. Liu, L. Liang, T. Yao, B. Pan, S. Wei and Y. Xie, *Nat. Commun.*, 2016, **7**, 12697.
164. L. Dai, Q. Qin, P. Wang, X. Zhao, C. Hu, P. Liu, R. Qin, M. Chen, D. Ou, C. Xu, S. Mo, B. Wu, G. Fu, P. Zhang and N. Zheng, *Sci. Adv.*, 2017, **3**, e1701069.
165. W. Zhang, Q. Qin, L. Dai, R. Qin, X. Zhao, X. Chen, D. Ou, J. Chen, T. T. Chuong, B. Wu and N. Zheng, *Angew. Chem. Int. Ed.*, 2018, **57**, 9475-9479.
166. S. Gao, X. Jiao, Z. Sun, W. Zhang, Y. Sun, C. Wang, Q. Hu, X. Zu, F. Yang, S. Yang, L. Liang, J. Wu and Y. Xie, *Angewandte Chemie International Edition*, 2016, **128**, 708-712.
167. S. Gao, Z. Sun, W. Liu, X. Jiao, X. Zu, Q. Hu, Y. Sun, T. Yao, W. Zhang, S. Wei and Y. Xie, *Nat. Commun.*, 2017, **8**, 14503.
168. F. Li, L. Chen, G. P. Knowles, D. R. MacFarlane and J. Zhang, *Angew. Chem. Int. Ed.*, 2017, **56**, 505-509.
169. S. Gao, Y. Lin, X. Jiao, Y. Sun, Q. Luo, W. Zhang, D. Li, J. Yang and Y. Xie, *Nature*, 2016, **529**, 68.
170. Z. Chen, K. Mou, X. Wang and L. Liu, *Angewandte Chemie International Edition*, 2018, **57**, 12790-12794.
171. H. Dong, L. Zhang, L. Li, W. Deng, C. Hu, Z.-J. Zhao and J. Gong, *Small*, 2019, **15**, 1900289.
172. Z. Sun, T. Ma, H. Tao, Q. Fan and B. Han, *Chem*, 2017, **3**, 560-587.
173. Z. Geng, X. Kong, W. Chen, H. Su, Y. Liu, F. Cai, G. Wang and J. Zeng, *Angew. Chem. Int. Ed.*, 2018, **130**, 6162-6167.